PERGAMON

Journal of Structural Geology 21 (1999) 1385–1405

JOURNAL OF STRUCTURAL GEOLOGY

www.elsevier.nl/locate/jstrugeo

Kinematic vorticity and tectonic significance of superposed mylonites in a major lower crustal shear zone, northern Fiordland, New Zealand

Keith A. Klepeis*, Nathan R. Daczko, Geoffrey L. Clarke

School of Geosciences, Division of Geology and Geophysics, Building F05, University of Sydney, Sydney, NSW 2006, Australia

Received 30 July 1998; accepted 9 April 1999

Abstract

New structural, metamorphic, finite strain and kinematic vorticity data from a 4 km-wide, subvertical shear zone in Fiordland, New Zealand reveal a history of deformation reflecting different tectonic regimes. An analysis of ductile fabrics within the shear zone and its wall rocks shows two distinctive stages of amphibolite facies mylonitic deformation (D_2^{ASZ} and D_3^{ASZ}) that are superimposed on older Paleozoic or early Mesozoic structures. Variations in strain intensity and well defined shear zone boundaries have allowed us to examine the progressive development of L_2^{ASZ}–S_2^{ASZ} and L_3^{ASZ}–S_3^{ASZ} fabrics and compare the types, kinematics and conditions of deformation that produced them. Mineral assemblages defining L_2^{ASZ}–S_2^{ASZ} provided calculated peak conditions of 11.9 ± 1.1 kbar and 581 ± 34°C indicative of lower crustal depths. Mineral assemblages defining L_3^{ASZ}–S_3^{ASZ} provided calculated peak conditions of 8.7 ± 1.2 kbar and 587 ± 42°C. Finite strain and kinematic vorticity studies show that D_2^{ASZ} involved ductile normal faulting and crustal thinning leading to decompression and exhumation of lower crustal rocks at some time during the Cretaceous rifting of ancestral New Zealand from Gondwana. D_3^{ASZ} represents an episode of mid-crustal dextral transpression that may have resulted from latest Mesozoic or Cenozoic oblique convergence. Reactivation of the subvertical S_3^{ASZ} foliation by cataclastic shear zones and brittle faults (D_4^{ASZ}) was accompanied by limited recrystallization at greenschist facies conditions. D_4^{ASZ} shear zones record upper crustal dextral strike-slip faulting that resembles late Tertiary deformation patterns associated with the Australian–Pacific transform plate boundary.

1. Introduction

Interpreting the tectonic significance of superposed ductile fabrics in shear zones is an important tool for unravelling the progressive evolution of multiply deformed regions. However, many interpretations are subject to simplifying assumptions such as the application of simple shear models to shear zone deformation or interpreting the origin of superposed fabrics in terms of a single progressive event. Many large-scale continental shear zones record multiple displacements reflecting changing tectonic regimes and conditions (e.g. Klepeis and Lawver, 1996; Klepeis et al., 1998). To avoid possible misinterpretations, objective criteria for distinguishing between different and changing styles of deformation using fabric elements in shear zones are needed.

One major ductile shear zone whose overall tectonic significance has been the subject of considerable debate is the Anita Shear Zone (Hill, 1995a, b), located in northern Fiordland, New Zealand (Figs. 1 and 2). This shear zone is 3.5–4 km-wide and is dominated by a steep to subvertical, NNE-striking foliation. Paleozoic, low–medium P, kyanite-bearing metasediments and orthogneisses occur to the west of the shear zone (Wood, 1972; Gibson, 1990; Blattner, 1991). Cretaceous high-P (~12–13 kbar) granulite facies assemblages and metabasic to metadioritic plutons occur to the east (Mattinson et al., 1986; Bradshaw,

* Corresponding author.
E-mail address: kklepeis@mail.usyd.edu.au (K.A. Klepeis)

0191-8141/99/$ - see front matter
PII: S0191-8141(99)00091-7

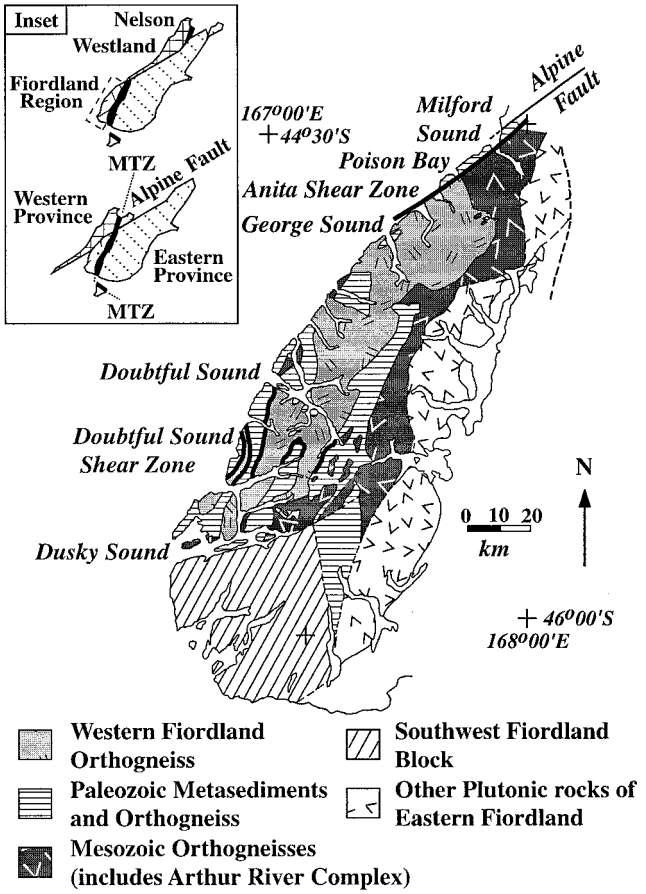

Fig. 1. Geological map of Fiordland showing major lithologic divisions (after Bradshaw, 1990). Note proximity of the Anita Shear Zone (bold, black line) to the Alpine fault (thin black line). Inset shows pre-Cenozoic configuration of the South Island which places the Westland–Nelson region adjacent to northern Fiordland (after Hill, 1995a, 1995b).

1989). Previous work (Blattner, 1991; Hill, 1995a, b) has shown that the Anita Shear Zone comprises superposed foliations displaying mylonitic to cataclastic textures reflecting conditions ranging from upper amphibolite to greenschist facies metamorphism. Excellent exposure of structural relationships along two fjords that transect the Anita Shear Zone and its wall rocks provide us with an opportunity to examine in detail the kinematic development of these superposed foliations and assess their overall tectonic significance using a variety of different techniques.

Much of the controversy surrounding the tectonic significance of this shear zone results from conflicting interpretations of the progressive development of shear zone fabrics and their kinematics. Wood (1972) originally interpreted the shear zone as a deep crustal segment of the nearby Alpine fault (Figs. 1 and 2). This interpretation was based on the steep to subvertical orientation of mylonitic foliations and their proximity to the southernmost exposed segment of the late Tertiary Alpine fault (dextral strike-slip). The Alpine fault is located several kilometers north and west of Milford Sound and strikes offshore approximately parallel to the overall NNE trend of the Anita Shear Zone (Figs. 1 and 2). Blattner (1991) suggested that the shear zone may represent a late Mesozoic or early Cenozoic transpressional precursor of the late Tertiary Alpine fault on the basis of a dextral shear sense, its steep orientation and its proximity to and parallelism with the trace of the Alpine fault. Hill (1995a, b) interpreted the Anita Shear Zone as part of a regional Cretaceous extensional shear zone system that included the subhorizontal Doubtful Sound Shear Zone (Gibson et al., 1988) in central Fiordland (Fig. 1) and the Paparoa metamorphic core complex (Tulloch and Kimbrough, 1989) north of Fiordland in the Nelson–Westland region (inset, Fig. 1). This interpretation was based on (1) evidence that the original geometry of the Anita Shear Zone may have been similar to the subhorizontal Doubtful Sound Shear Zone, and was later modified to its present steep orientation by younger folds (Hill, 1995a, b) and (2) the relative proximity of northern Fiordland to the mid-Cretaceous extensional Paparoa metamorphic core complex after reconstructing the region to its pre-Cenozoic configuration (inset, Fig. 1). One problem with this extensional model, however, was the absence of metamorphic evidence for decompression similar to that observed in the Nelson–Westland and central Fiordland regions and uncertainties about how the youngest phases of deformation had modified older structures in the shear zone. These different interpretations have led to disparities regarding the role of extensional, contractional and strike-slip styles of deformation in the tectonic development of lower crustal exposures in northern Fiordland.

In this paper, we present new structural, metamorphic, finite strain and kinematic vorticity data that help constrain the nature of superposed fabrics in the Anita Shear Zone. Our approach was to apply a wide range of different techniques to the analysis of the shear zone structures to determine the types, geometries, kinematics and conditions of deformation that produced them. Outcrop-scale variations in strain intensity (subzones are tens of meters wide) allowed us to compare and contrast analyses of areas affected by different degrees of deformation *in precisely the same lithology*. This enabled us to compare directly different data sets without the complicating effects of changing physical properties between different lithologies or protolith compositions. In addition, clear crosscutting relationships, well-defined shear zone boundaries, and the spatial variations in strain intensity allowed us to reconstruct the progressive development of different stages of deformation. Finally, areas affected by different degrees of deformation contain a relatively homo-

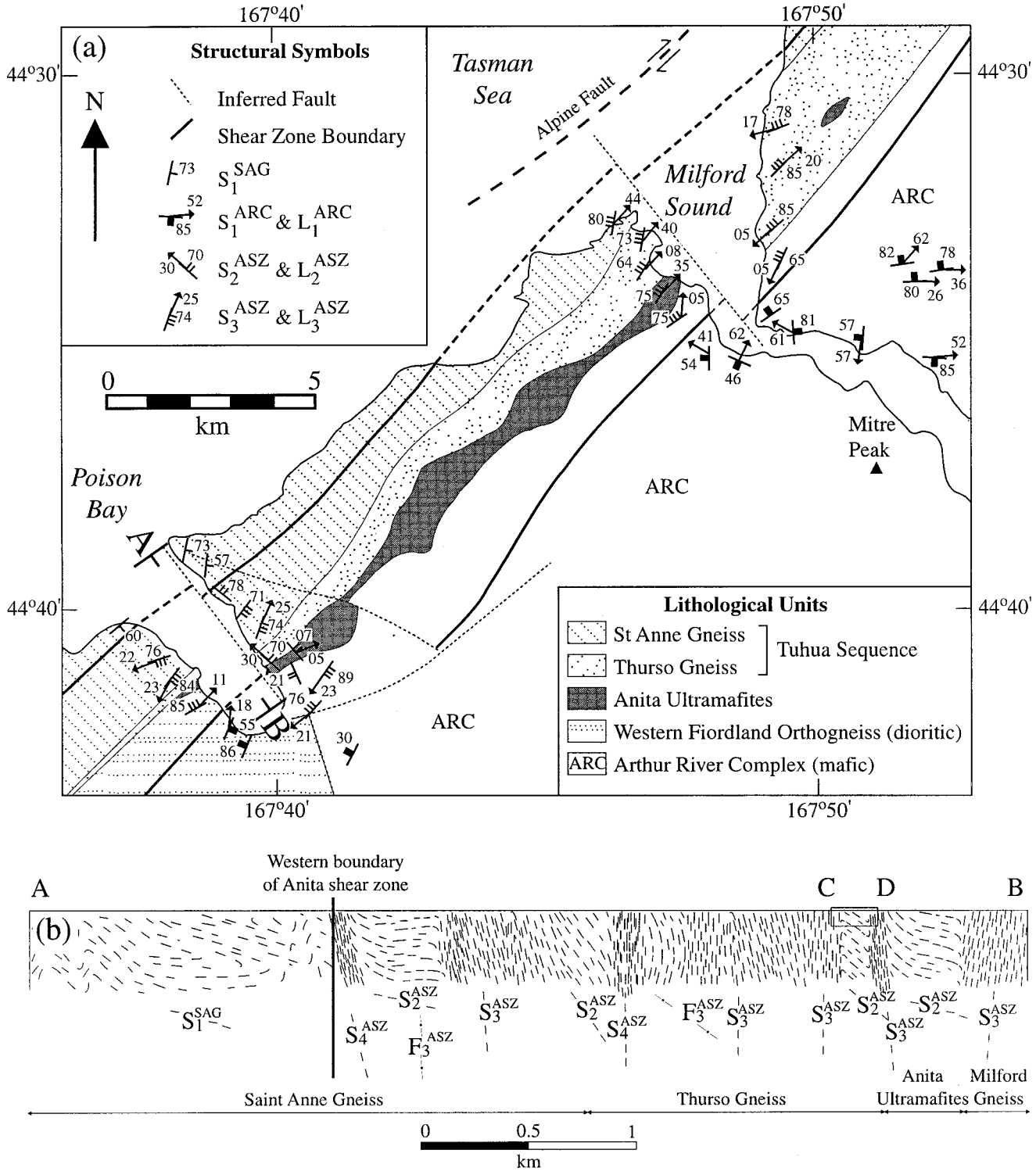

Fig. 2. (a) Structural map of the Anita Shear Zone showing major lithologic units within and outside the shear zone boundaries (bold lines). (b) Cross-section (A–B) constructed for northern shore of Poison Bay showing regional-scale variations in the occurrence and orientation of different foliations within and outside the shear zone. See text for discussion. Cross-section (C–D) is shown in Fig. 7.

geneous metapsammite unit containing well preserved microstructures and rotated porphyroclast systems that are especially well suited for kinematic vorticity analyses.

Our results indicate that three distinctive fabric forming events (D_2^{ASZ}, D_3^{ASZ}, D_4^{ASZ}) produced the Anita Shear Zone since the early Cretaceous. An early, gently SE-dipping mylonitic fabric (L_2^{ASZ}–S_2^{ASZ}) preserves evidence for mid-Cretaceous lower crustal thinning and simple shear-dominated ductile normal faulting. A younger steep to subvertical pure shear-dominated transpressional fabric (L_3^{ASZ}–S_3^{ASZ}) preserves evidence for late Mesozoic or Cenozoic mid-crustal dextral displacements at high angles to the L_2^{ASZ} transport direction. The steeply dipping S_3^{ASZ} foliation was subsequently reactivated by semi-brittle, greenschist facies dextral strike-slip faults (D_4^{ASZ}) that may be related to late Cenozoic Alpine deformation.

2. Regional geologic history

Paleozoic metasedimentary rocks and metagranitic orthogneisses that now lie west and south of the Anita Shear Zone (Fig. 1) preserve a history of mid-Paleozoic convergent margin deformation, low- to high-grade metamorphism and arc-related plutonism that occurred along the Pacific margin of Gondwana (Wood, 1972; Carter et al., 1974; Hill, 1995a; Ireland and Gibson, 1998). U–Pb microprobe dates (Ireland and Gibson, 1998), Rb–Sr isochron ages (Oliver, 1980) and K–Ar cooling ages (Gibson et al., 1988) indicate that this Paleozoic tectonism lasted from ~481 to ~334 Ma (Gibson et al., 1988; Gibson and Ireland, 1996). A polyphase tectonic history during this period is reflected in early low-*P*–high-*T*, sillimanite-bearing mineral assemblages that are overprinted by medium- to high-*P*, kyanite-bearing assemblages (Gibson et al., 1988; Gibson, 1990; Ireland and Gibson, 1998).

Superimposed on Paleozoic events in Fiordland is a younger record of high grade metamorphism, deformation and arc-related plutonism that began in the Triassic and lasted into the early Cretaceous (Bradshaw, 1989; Tulloch and Kimbrough, 1989; Mortimer, 1993; Brown, 1996). This period of Mesozoic tectonism coincided with the accretion of numerous volcano-sedimentary terranes onto the Pacific margin of Gondwana (Mattinson et al., 1986; McCulloch et al., 1987; Tulloch and Kimbrough, 1989) and resulted in the emplacement of a regionally extensive, 126–119 Ma dioritic to monzodioritic batholith (Mattinson et al., 1986; Bradshaw, 1989). The roots of this batholith are now represented by the Western Fiordland orthogneiss (Fig. 1, WFO). Batholith emplacement was followed by high-*P* granulite facies metamorphism peaking at temperatures of 650–700°C and pressures of 12–13 kbar (Bradshaw, 1989). East of the Anita Shear Zone, the WFO is hosted by the Arthur River Complex (ARC, Fig. 2), a heterogeneous assemblage of mafic to dioritic orthogneisses of uncertain protolith age (Mattinson et al., 1986; Bradshaw, 1990; Gibson and Ireland, 1995). This complex is subdivided into the relatively homogeneous Milford Gneiss, which forms the eastern wall rock of the Anita Shear Zone, and the banded Harrison Gneiss exposed farther east.

High-*P* metamorphism contemporaneous with emplacement of the WFO was followed by widespread continental extension associated with the breakup of the Pacific margin of Gondwana (Tulloch and Kimbrough, 1989). In central Fiordland, the WFO is deformed by the Doubtful Sound Shear Zone, a gently dipping mylonitic zone that was originally interpreted as a ductile thrust fault (Oliver and Coggon, 1979; Oliver, 1980) but reinterpreted as a major extensional detachment fault by Gibson et al. (1988). A U–Pb zircon age of ~119 Ma and K–Ar amphibole and biotite cooling ages of ~93 and ~77 Ma, respectively, support a mid-Cretaceous age for the Doubtful Sound Shear Zone (Gibson and Ireland, 1995). Hill (1995a, b) correlated the subvertical foliation of the Anita Shear Zone with the subhorizontal foliation of the Doubtful Sound Shear Zone and interpreted a similar extensional kinematic evolution and a mid-Cretaceous age for its development. This late Mesozoic extensional regime is inferred to have controlled the exhumation of the lower crustal roots of the early Mesozoic arc (Gibson and Ireland, 1995). By late Tertiary time, changes in relative plate motions led to development of the modern Australian–Pacific transform plate boundary (Sutherland, 1995; Lamarche et al., 1997). In southern New Zealand (Fig. 1) this plate boundary is represented by the dextral transpressional Alpine Fault (Norris et al., 1990).

3. Structure of the Anita Shear Zone

Two fjords, Milford Sound and Poison Bay (Fig. 2), provide nearly continuous exposure across the Anita Shear Zone and its wall rocks along sections oriented orthogonal to its NNE strike. Milford Sound exposes the eastern boundary of the shear zone, whereas Poison Bay contains exposures of both its western and eastern boundaries. For the purposes of this paper, we divide the structure of the Anita Shear Zone into three domains: (1) the eastern wall rock of the shear zone, (2) the western wall rock of the shear zone, and (3) all structures located between the eastern and western boundaries of the shear zone. In this section, we define the structural elements that comprise the shear zone and its wall rocks and describe the main features that

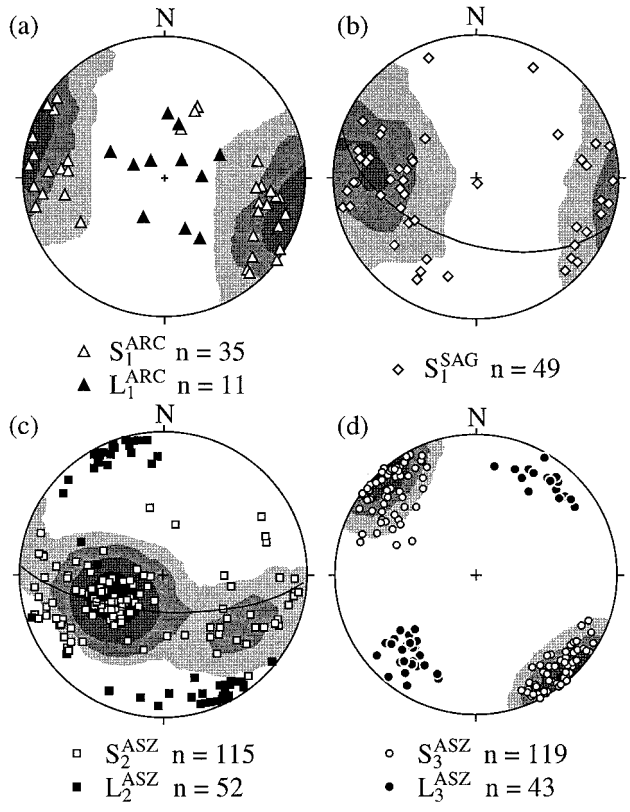

Fig. 3. Lower hemisphere equal area stereoplots of structural data from Milford Sound and Poison Bay. Contour intervals are 3% per 1% area. (a) Pre-Anita Shear Zone structural elements (poles to S_1^{ARC} and L_1^{ARC}) from the Arthur River Complex located east of the eastern boundary of the shear zone at Milford Sound. (b) Pre-Anita Shear Zone structural elements (poles to S_1^{SAG}) from the Saint Anne Gneiss located west of the western boundary of the Anita Shear Zone at Poison Bay. (c) D_2^{ASZ} structural elements (poles to S_2^{ASZ} and L_2^{ASZ}) within the shear zone at Poison Bay. (d) D_3^{ASZ} structural elements (poles to S_3^{ASZ} and L_3^{ASZ}) within the shear zone at Milford Sound and Poison Bay. See text for discussion.

define its subvertical western and eastern boundaries. We use the superscript *ASZ* to distinguish deformation that produced Anita Shear Zone structures and the superscripts *ARC* and *SAG* to distinguish structures that pre-date the shear zone in the Arthur River Complex and Saint Anne Gneiss (Fig. 2) east and west of the shear zone, respectively.

3.1. Shear zone boundaries and D_1 fabric elements outside the shear zone

The eastern boundary of the Anita Shear Zone at Milford Sound (Fig. 2) lies within relatively homogeneous mafic and intermediate orthogneisses of the Milford Gneiss. To the east of and outside the shear zone, these rocks preserve a complex history of deformation and, in places, high pressure (12–13 kbar) granulite facies metamorphism (Blattner, 1991). Near the shear zone, the dominant foliation in these gneisses (S_1^{ARC}) is defined by aligned aggregates of amphibole, plagioclase, clinozoisite, rutile with or without garnet, clinopyroxene and biotite. The orientation of S_1^{ARC} is variable but generally strikes northerly and displays moderate to steep dips to the east and west (Fig. 3a). A weakly to strongly developed, down-dip mineral lineation (L_1^{ARC}) defined by aligned amphibole, clinopyroxene, and clinozoisite, ±biotite occurs on S_1^{ARC} foliation planes. L_1^{ARC} displays variable trends but generally plunges moderately to steeply down-dip (Fig. 3a).

The eastern boundary of the Anita Shear Zone is marked by a narrow 1–2 m-wide, NNE-striking subvertical zone where the L_1^{ARC}–S_1^{ARC} fabric is sharply truncated and overprinted by steep to subvertical mylonitic foliations of the Anita Shear Zone (shear zone fabrics are described below). West of this boundary, L_1^{ARC}–S_1^{ARC} in the Milford Gneiss is completely recrystallized and transposed by shear zone mylonitization. A pronounced reduction in average grain size accompanies this transposition. On the basis of foliation orientation, texture, grain size, mineral assemblages and overprinting relationships, elements of the Anita Shear Zone are easily distinguished from those that occur to the east.

At Poison Bay, the eastern boundary of the Anita Shear Zone lies within metadioritic rocks of the Western Fiordland orthogneiss (Fig. 2). West of this boundary and within the shear zone the metadiorite is a well lineated, well foliated, amphibole-dominated schist. East of this boundary, the rock displays compositional banding and retains a two pyroxene igneous assemblage that was recrystallized under high-grade metamorphic conditions. An anastomosing foliation outside the shear zone is defined in places by aligned quartz, plagioclase, rutile and aggregates of garnet and clinopyroxene. A weak N-plunging mineral lineation outside the shear zone is defined by quartz–feldspar aggregates and aligned pyroxene grains. For the purposes of this paper, we group these structures together with the L_1^{ARC}–S_1^{ARC} fabric in the Milford Gneiss because both are overprinted by the shear zone mylonites. We do not intend to imply, however, that the structures in the WFO and Milford Gneiss were coeval.

The western boundary of the Anita Shear Zone at Poison Bay lies within the Paleozoic (protolith age) Saint Anne Gneiss (Fig. 2). This unit comprises interlayered metapelitic and metapsammitic rocks with rare mafic layers and minor felsic to mafic dikes and plutons. West of the Anita Shear Zone, the dominant structure in these rocks is bedding (S_0). A weakly developed foliation defined by lenticular aggregates of quartz + plagioclase and aligned flakes of muscovite + biotite parallels bedding planes. This composite S_0/S_1^{SAG} foliation is tightly folded by

upright NE-plunging folds (F_2^{SAG}) and generally strikes north (Fig. 3b). Mineral lineations within the rocks outside the shear zone are rare to absent. Kyanite grains are not aligned within foliation planes suggesting static metamorphic growth. One or two other weakly developed foliations may also occur within this rock in some localities (Hill, 1995b). Because all of these foliations and the F_2^{SAG} folds are overprinted and deformed by the Anita Shear Zone mylonites, we group these structures together as part of pre-shear zone D_1^{SAG} deformation.

The western boundary of the Anita Shear Zone is marked by a subvertical zone up to several hundred meters wide. Here, as on the eastern side, subvertical mylonites that form the Anita Shear Zone truncate and transpose all older foliations that occur in its wall rocks. However, the western boundary is much more diffuse than the eastern boundary. We attribute this diffuse nature to a weaker rheology compared to the mafic to intermediate orthogneisses on the east. Also unlike the eastern side, rocks in the western boundary zone are affected by a series of tight to isoclinal folds (F_3^{ASZ}) that post-date the F_2^{SAG} folds. These F_3^{ASZ} folds increase in abundance toward the center of the Anita Shear Zone. Numerous steeply dipping, greenschist facies mylonites and minor cataclastic shear zones also occur within 100 m of the boundary zone.

3.2. Structural elements within the Anita Shear Zone

The Anita Shear Zone contains at least three generations of superposed foliations and lineations (L_2^{ASZ}–S_2^{ASZ}, L_3^{ASZ}–S_3^{ASZ}, L_4^{ASZ}–S_4^{ASZ}) that are easily distinguished on the basis of orientation, texture, microstructure and metamorphic mineral assemblage. Crosscutting relationships between these superposed fabrics are exceptionally well preserved at Poison Bay. Within the Anita Shear Zone and along its eastern and western boundaries are narrow, 1–1.5 km-wide zones of highly deformed and recrystallized Arthur River Complex orthogneisses and Saint Anne paragneisses, respectively. Two other lithologies lie at the center of the shear zone: the Thurso Gneiss and the Anita ultramafite (Fig. 2). The Thurso Gneiss is a heterogeneous package of calcsilicate to mafic gneiss, marble, and metapsammitic schist. East of the Thurso Gneiss, the Anita ultramafite separates the Paleozoic metasedimentary rocks from orthogneisses of the Arthur River Complex. These rocks form a narrow 1-km-wide zone of highly deformed, boudinaged and serpentinized harzburgites, dunites, and pyroxenites of unknown origin.

The oldest recognizable foliation within the Anita Shear Zone is a subhorizontal to gently east- or west-dipping compositional layering in the Thurso Gneiss. This compositional layering probably represents deformed and metamorphosed bedding. Supporting this interpretation, we observed a narrow (< 1 m) metaconglomerate layer, complete with cobble size clasts, that parallels the subhorizontal compositional layering in the Thurso Gneiss (Fig. 4a).

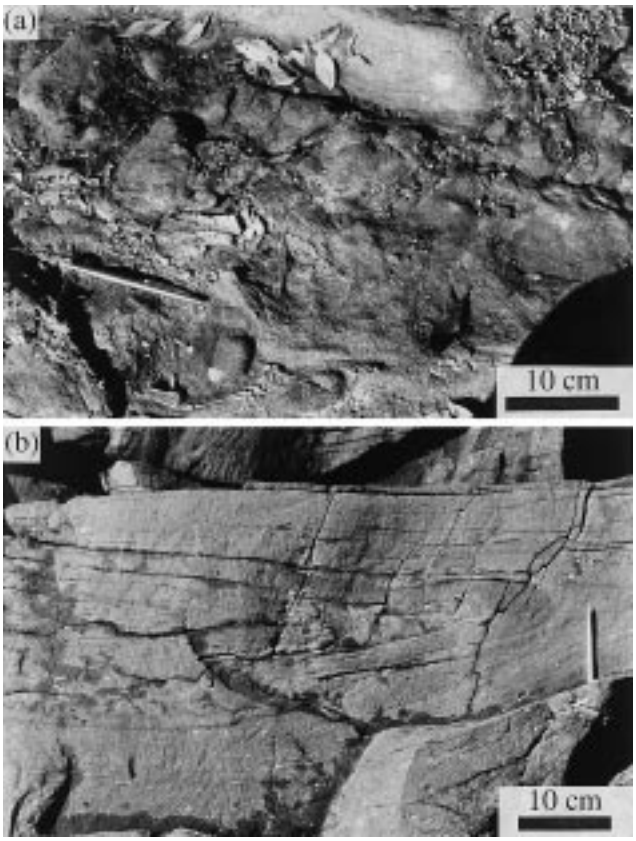

Fig. 4. (a) A deformed metaconglomerate layer with cobble-size clasts parallel to compositional layering in metapsammites located within a D_2^{ASZ} strain domain at Poison Bay. Outcrop was used in finite strain analysis Table 1. (b) Recumbent F_2^{ASZ} fold of a mafic layer in D_2^{ASZ} strain domain at Poison Bay. Pebble-size feldspar porphyroclasts are common in the psammitic layers above and below the fold.

Compositional layering within the Thurso and Saint Anne gneisses is intensely deformed into tight to isoclinal, recumbent to inclined, gently NE-plunging folds (F_2^{ASZ}, Fig. 4b). Many of these F_2^{ASZ} folds are rootless and all have axial planes that lie parallel to a gently to moderately dipping mylonitic to ultramylonitic foliation (S_2^{ASZ}). S_2^{ASZ} represents the first phase of intense mylonitic deformation that occurred within the Anita Shear Zone. In the Thurso and Saint Anne gneisses S_2^{ASZ} is defined by the assemblage garnet, biotite, plagioclase, quartz, amphibole, clinozoisite and rutile. In the Anita ultramafites, S_2^{ASZ} is defined by flattened and recrystallized olivine and talc grains, and in the Milford Gneiss, it is defined by aligned quartz–plagioclase aggregates, clinozoisite, ilmenite and amphibole. A penetrative, gently to moderately NNW- and SSE-plunging mineral lineation (L_2^{ASZ}) occurs on S_2^{ASZ} foli-

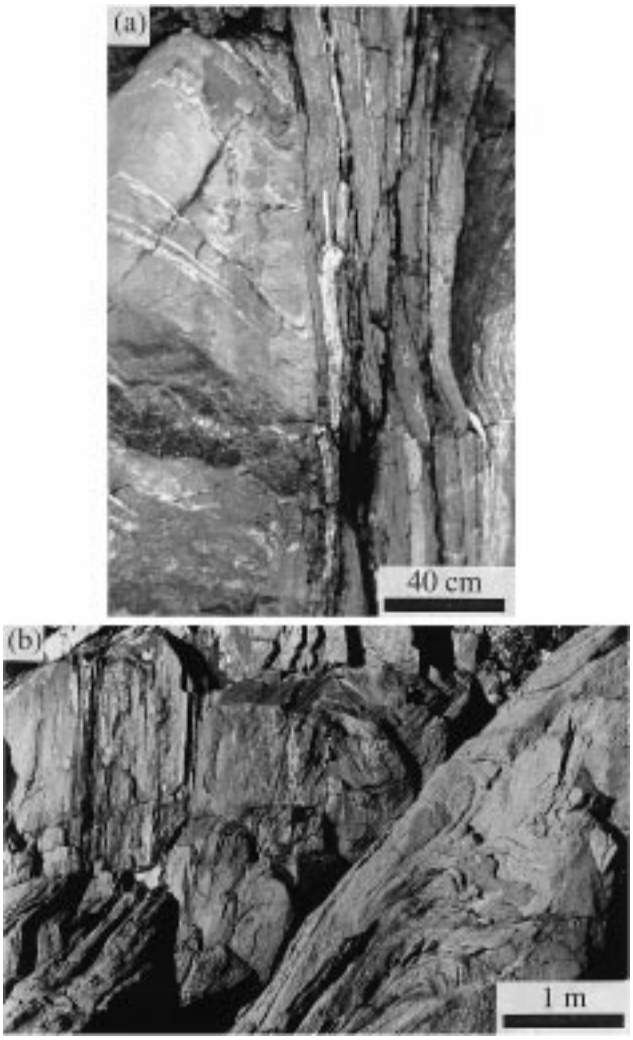

Fig. 5. (a) View of a vertical section of outcrop showing a gently SE-dipping (to the right) S_2^{ASZ} foliation sharply truncated by a vertical S_3^{ASZ} foliation at Poison Bay. (b) View of an intermediate strain domain located between a D_3^{ASZ} strain domain (left) and a D_2^{ASZ} strain domain (right) within the Anita Shear Zone at Poison Bay. At the right-center of the photograph a recumbent F_2^{ASZ} fold with an axial planar S_2^{ASZ} foliation is refolded by an open, gently inclined F_{3a}^{ASZ} fold (see Fig. 6b for interpretation). F_{3b}^{ASZ} folds in D_3^{ASZ} strain domain to left are upright, tight to isoclinal with axial planes parallel to a subvertical S_3^{ASZ} foliation.

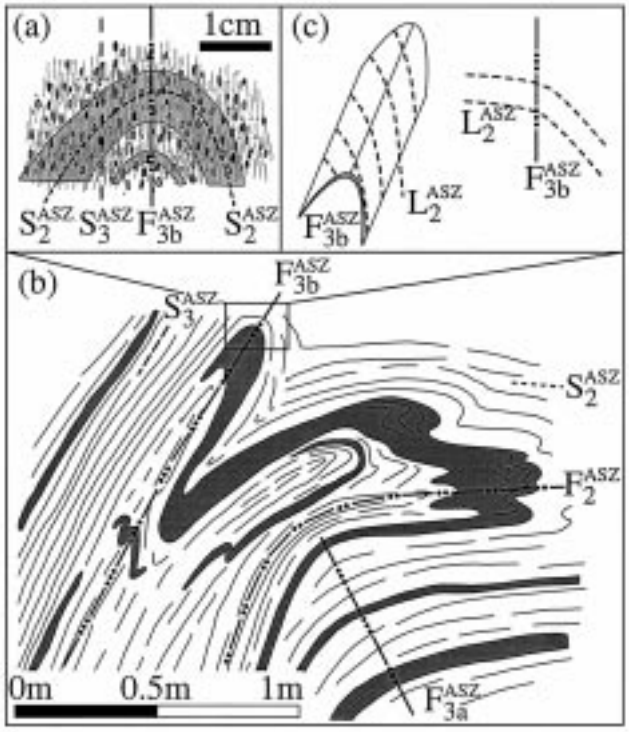

Fig. 6. (a) Sketch of thin section showing upright F_{3b}^{ASZ} fold of S_2^{ASZ} with a subvertical axial planar S_3^{ASZ} foliation from a D_3^{ASZ} domain of the shear zone. (b) Sketch of a portion of the photograph shown in Fig. 5(b) showing a type III fold interference pattern resulting from the refolding of a recumbent F_2^{ASZ} fold by an upright (F_{3b}^{ASZ}) and an inclined (F_{3a}^{ASZ}) fold from within an intermediate strain domain. To left in D_3^{ASZ} strain domain, S_3^{ASZ} parallels F_{3b}^{ASZ} fold axial planes. (c) The unfolding of L_2^{ASZ} around F_{3b}^{ASZ} fold axes shows a curved pattern indicative of minor fold axis rotation during D_3^{ASZ}.

ation planes within the shear zone (Fig. 3c). The boudinage of older pegmatites and mafic dikes indicates that L_2^{ASZ} is a true stretching lineation. These lineations are defined by aligned amphibole in the Milford Gneiss, aligned amphibole, clinozoisite and biotite in the Paleozoic rocks and stretched olivine in the Anita ultramafites. The orientation of L_2^{ASZ}–S_2^{ASZ} within the shear zone sharply contrasts with the orientation of structural elements produced during D_1^{SAG} and D_1^{ARC} and measured outside of the Anita Shear Zone (compare Fig. 3a, b and c).

Overprinting the gently to moderately-dipping L_2^{ASZ}–S_2^{ASZ} fabric in the Anita Shear Zone, is a subvertical, NNE-striking mylonitic foliation (S_3^{ASZ}). This foliation truncates and transposes the older L_2^{ASZ}–S_2^{ASZ} fabric, in places forming at right angles (Fig. 5a). In the Thurso and Saint Anne Gneisses, S_3^{ASZ} is defined by flattened and aligned garnet, plagioclase, quartz, amphibole, biotite, clinozoisite and titanite. In the Milford Gneiss, S_3^{ASZ} is defined by the assemblage plagioclase, quartz, amphibole, epidote and titanite. Titanite, which is characteristic of the S_3^{ASZ} assemblage, does not occur within the S_2^{ASZ} assemblage anywhere in the shear zone. A penetrative mineral lineation, defined by aligned amphibole in the Milford Gneiss and aligned biotite, amphibole and quartz–plagioclase aggregates in the Thurso and Saint Anne Gneisses, is everywhere associated with S_3^{ASZ}. L_3^{ASZ} is subhorizontal to gently NE- or SW-plunging at high to near orthogonal angles to the L_2^{ASZ} mineral lineation (Fig. 3d). Boudinaged mafic layers within the Milford and Thurso Gneisses and a macroscopic pinch and swell of the Anita ultramafite (Fig. 2), indicate that L_3^{ASZ} is also a true stretching lineation. The L_3^{ASZ}–S_3^{ASZ} fabric parallels both boundaries of the

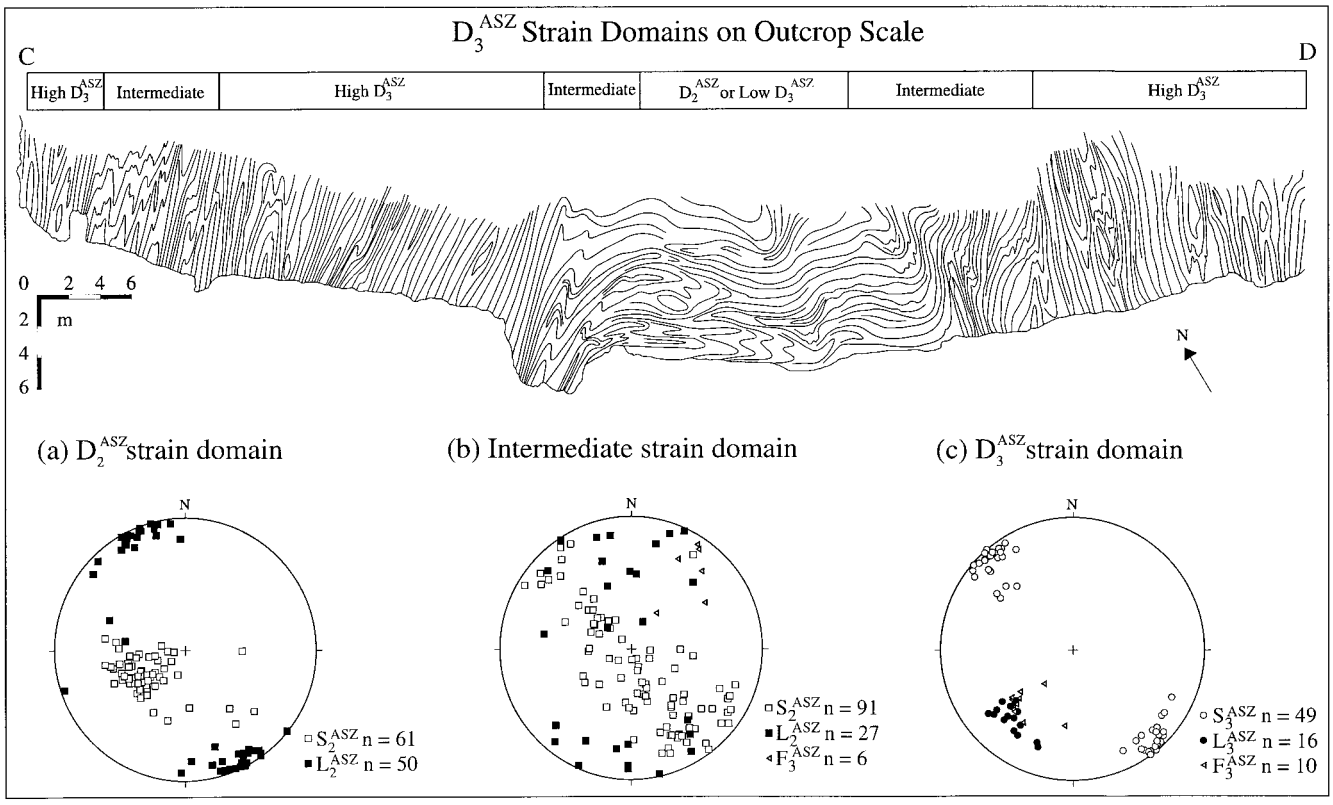

Fig. 7. NW–SE cross-section (location C–D shown in Fig. 2b) showing foliation trajectories at outcrop site 97106 at Poison Bay. Foliation trajectories show the changing orientations and geometries of D_2^{ASZ} and D_3^{ASZ} mylonites within the shear zone. Strain domains, defined in the text, are correlated with the occurrence and geometry of L_2^{ASZ}–S_2^{ASZ} and L_3^{ASZ}–S_3^{ASZ} fabrics. D_2^{ASZ} zones show a weakly folded (F_3^{ASZ}) subhorizontal L_2^{ASZ}–S_2^{ASZ} mylonitic fabric. D_3^{ASZ} domains show a subvertical L_3^{ASZ}–S_3^{ASZ} mylonitic fabric. Intermediate strain domains show an intermediate degree of F_3^{ASZ} fold development where refolded folds are visible (see Figs. 5b and 6b). (a) Plot of L_2^{ASZ} and poles to S_2^{ASZ} from D_2^{ASZ} strain domains. (b) Plot of L_2^{ASZ}, F_3^{ASZ} axes, and poles to S_2^{ASZ} from intermediate strain domains. (c) Plot of L_3^{ASZ}, F_3^{ASZ} axes, and poles to S_3^{ASZ} from D_3^{ASZ} strain domains. All plots are lower hemisphere equal area projections.

shear zone and is the most penetrative fabric in the shear zone. Across the entire width of the Anita Shear Zone, S_3^{ASZ} occurs together with upright to gently inclined, NE- and SW-plunging folds (F_3^{ASZ}) of S_2^{ASZ} (Figs. 5b, 6 and 7). The interlimb angles of these folds vary from open to isoclinal within the shear zone. Type III (fishhook) interference patterns resulting from superposed F_3^{ASZ} on F_2^{ASZ} folds are visible in areas where the S_3^{ASZ} foliation was weakly developed (Figs. 5b and 6b).

The youngest phase of deformation within the Anita Shear Zone (D_4^{ASZ}) produced narrow (< 10 m) subvertical greenschist facies shear zones that crosscut D_2^{ASZ} and D_3^{ASZ} structures. These minor shear zones are distinguished from D_3^{ASZ} mylonites on the basis of mineral assemblage (S_4^{ASZ} is dominated by muscovite), the occurrence of cataclastic textures and a crenulation cleavage in pelitic schists, and crosscutting relationships. D_4^{ASZ} is best developed in the Saint Anne Gneiss near the western boundary of the shear zone and on both sides of the Anita ultramafite. Within the Saint Anne Gneiss, S_4^{ASZ} is defined almost entirely by coarse-grained muscovite. Near the ultramafite D_4^{ASZ} structures are steep, NNE-striking brittle fault zones that contain subhorizontal slickenlines on fault planes. Cataclastic textures, intensely fractured olivine grains and talc in the Anita ultramafites, and fractured garnet, epidote and chlorite in the Milford Gneiss are visible in thin section. Numerous other brittle faults (D_4^{ASZ}) offset lithological contacts and the shear zone boundaries (Fig. 2). These faults are parallel and slightly oblique to the walls of Milford Sound and Poison Bay.

4. Finite strain analysis

In this section, we present two measures of spatial variations in finite strain within the Anita Shear Zone and correlate these variations with differences in the geometry and occurrence of the superposed L_2^{ASZ}–S_2^{ASZ} and L_3^{ASZ}–S_3^{ASZ} fabrics. This analysis helped us to determine the effects of D_3^{ASZ} deformation on the evolution of the Anita Shear Zone and whether

it significantly differed from the type of deformation that produced the flat-lying L_2^{ASZ}–S_2^{ASZ} fabric. First, we subdivide the Anita Shear Zone into D_2^{ASZ} (low D_3^{ASZ}), intermediate and high D_3^{ASZ} strain domains by measuring variations in the tightness of F_3^{ASZ} folds in a direction perpendicular to the shear zone boundaries. Following the definition of different strain domains and gradients, we apply the methods of Lisle (1985) and De Paor (1988) to quantify and compare finite strain in D_2^{ASZ} and D_3^{ASZ} strain domains using deformed cobbles in a conglomerate layer and deformed porphyroclasts in metapsammites that occur within both domains.

4.1. Definition of strain domains and strain gradients

Within the Anita Shear Zone, spatial changes in F_3^{ASZ} fold geometry directly coincide with the following: (1) variations in both the occurrence and geometries of the L_2^{ASZ}–S_2^{ASZ} and L_3^{ASZ}–S_3^{ASZ} fabrics and (2) different equilibrium mineral assemblages. We discuss the different mineral assemblages in a later section. One of the best places to observe these relationships is at site 97106 at Poison Bay where variations in strain intensity occur over tens of meters in identical lithologies (Fig. 7). At this and other sites, we observed that in areas where the subhorizontal L_2^{ASZ}–S_2^{ASZ} fabric forms the dominant structure, S_3^{ASZ} and titanite are absent and F_3^{ASZ} folds are very weakly developed, occurring only as gently inclined, open warps of S_2^{ASZ} (Figs. 2 and 7). These areas, where the effects D_3^{ASZ} deformation are minimal to nil, we define as D_2^{ASZ} strain zones or, equivalently, areas of lowest D_3^{ASZ} strain (Figs. 2b and 7). Such zones occur across the entire width of the shear zone, ranging from several centimeters to 100 m wide in a direction perpendicular to the shear zone boundaries (Fig. 2b). In areas where the S_3^{ASZ} foliation is most intensely developed and completely truncates and transposes the older S_2^{ASZ} foliation (Fig. 5a and b), F_3^{ASZ} folds are upright, tight to isoclinal and extremely well developed. We define these areas as D_3^{ASZ} strain zones, representing areas where D_3^{ASZ} strain is the highest and includes the effects of D_3^{ASZ} superimposed on D_2^{ASZ}. In these zones, F_3^{ASZ} and S_3^{ASZ} occur together, S_3^{ASZ} everywhere parallels the axial planes of the F_3^{ASZ} folds, and F_3^{ASZ} axes parallel L_3^{ASZ} mineral lineations. Situated midway between D_3^{ASZ} and D_2^{ASZ} strain zones, are transitional areas where D_2^{ASZ} and D_3^{ASZ} structures occur together and clear overprinting relationships are visible. In some of these areas, S_3^{ASZ} clearly truncates S_2^{ASZ} (Fig. 5a). In other areas of intermediate strain (Figs. 5b and 7), S_3^{ASZ} overprints S_2^{ASZ} at high angles and L_2^{ASZ} and L_3^{ASZ} crosscut one another displaying trends 70–85° apart. In these intermediate strain areas, F_3^{ASZ} axes and L_3^{ASZ} mineral lineations occur at low angles to one another, and type III (fishhook) interference fold patterns occur between upright to gently inclined F_3^{ASZ} folds and recumbent isoclinal F_2^{ASZ} folds (Figs. 5b and 6b). Site 97106 (Fig. 7) illustrates the progressive change in the geometry of D_2^{ASZ} and D_3^{ASZ} structural elements from D_2^{ASZ} to intermediate D_3^{ASZ} strain areas across a section several tens of meters wide. We have used these variations in F_3^{ASZ} fold development to measure the amount of shortening by F_3^{ASZ} folding in a direction perpendicular to the shear zone boundaries using the simple method of measuring the final vs initial lengths of folded S_2^{ASZ} surfaces. These measurements suggest that, in some small areas of high D_3^{ASZ} strain zones, >70% shortening by F_3^{ASZ} folding occurred perpendicular to the shear zone boundaries during D_3^{ASZ}. In contrast, some parts of the low strain areas have been affected by as little as 7% shortening by F_3^{ASZ} folding. This result simply provides us with

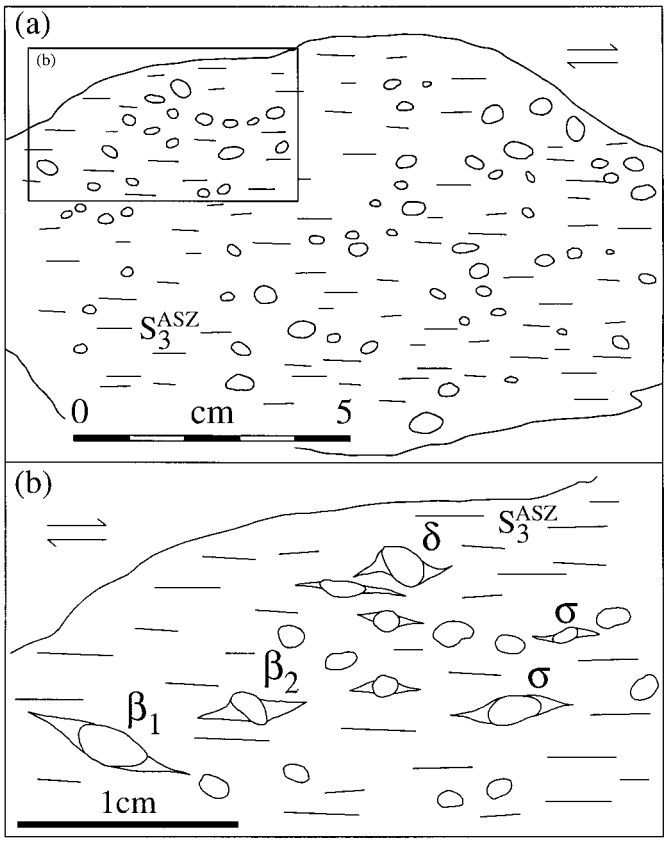

Fig. 8. (a) Representative sketch of outcrop photograph showing the uniform distribution of pebble-size rotated feldspar porphyroclasts in a deformed metapsammite sample from site 97106 at Poison Bay. Clasts show a wide variety of orientations, many show a preferred alignment parallel to S_3^{ASZ}. (b) Sketch of photograph from box shown in (a). Sketch shows geometries of recrystallized tails on rotated feldspar clasts. Four main types of rotated clasts are shown: (i) forward-rotated (dextral) σ-type; (ii) forward-rotated (dextral) δ-type; (iii) backward-rotated (sinistral) σ-type (β_1); and (iv) backward-rotated (dextral) σ-type with tails attached to the broad side of the clast (β_2). See text for discussion of microstructure.

Table 1
Summary of finite strain data[a,b,c]

Strain domain	Scale	Clast type	AP	n	H	I_{sym}	χ^2	R_s	$R*_s$	$R_s^{\wedge}$	$\chi^{2\wedge}$
D_2^{ASZ}	Thin-section	Feldspar	*XZ*	40	1.92	0.95	1.88	1.50	1.60	1.56	70.70
D_2^{ASZ}	Thin-section	Feldspar	*XY*	30	1.50	0.93	2.33	1.35	1.30	1.30	54.00
D_2^{ASZ}	Thin-section	Feldspar	*YZ*	40	1.59	0.70	3.25	1.30	1.26	1.28	50.08
D_2^{ASZ}	Outcrop	Quartz and feldspar	*XZ*	34	1.89	0.76	1.87	1.70	1.62	–	–
D_2^{ASZ}	Outcrop	Quartzite cobbles	*XZ*	32	1.98	0.94	3.70	1.80	1.80	–	–
D_3^{ASZ}	Sub-thin-section	Feldspar	*XZ*	32	1.67	0.82	3.31	1.45	1.44	1.40	56.87
D_3^{ASZ}	Sub-thin-section	Feldspar	*XY*	38	1.39	0.79	5.42	1.05	1.06	1.09	39.68
D_3^{ASZ}	Sub-thin-section	Feldspar	*YZ*	21	1.52	0.83	3.17	1.20	1.27	1.23	38.14
D_3^{ASZ}	Thin-section	Feldspar	*XZ*	32	1.60	0.94	0.81	1.40	1.43	1.35	55.75
D_3^{ASZ}	Thin-section	Feldspar	*XY*	34	1.42	0.82	0.71	1.15	1.18	1.15	39.55
D_3^{ASZ}	Thin-section	Feldspar	*YZ*	34	1.60	0.65	3.94	1.15	1.16	1.20	21.06
D_3^{ASZ}	Thin-section	Feldspar	*XZ*	40	1.69	0.65	0.81	1.60	1.60	1.50	11.30
D_3^{ASZ}	Thin-section	Feldspar	*XY*	38	1.43	0.79	1.21	1.15	1.16	1.16	62.42
D_3^{ASZ}	Thin-section	Feldspar	*YZ*	40	1.49	0.75	2.06	1.25	1.24	1.28	50.00
D_3^{ASZ}	Hand sample	Quartz and feldspar	*XZ*	34	1.64	0.94	5.64	1.45	1.40	1.46	86.00
D_3^{ASZ}	Hand sample	Quartz and feldspar	*XZ*	40	1.69	0.90	2.06	1.50	1.52	1.44	81.50
D_3^{ASZ}	Outcrop	Quartz and feldspar	*XZ*	38	1.64	0.68	2.79	1.30	1.22	–	–

[a] AP = analysis plane; n = sample number.
[b] Lisle (1985): H = harmonic mean of R_f values; I_{sym} = index of symmetry (critical value is 0.51); χ^2 = statistical χ^2 test result (critical value is 5.991); R_s = estimated tectonic strain ratio.
[c] De Paor (1988): $R*_s$ = estimated tectonic strain ratio (hand plot); $R_s^{\wedge}$ = estimated tectonic strain ratio (computer plot); $\chi^{2\wedge}$ = statistical χ^2 test result (small values indicated a better result — computer plot).

an objective means of defining variations in D_3^{ASZ} strain intensity and correlating observed changes in L_2^{ASZ}–S_2^{ASZ} and L_3^{ASZ}–S_3^{ASZ} fabric geometries at the outcrop scale with these variations. We do not imply that >70% shortening occurred across the entire shear zone.

A comparison of the geometry of F_3^{ASZ} folds in D_2^{ASZ}, intermediate and D_3^{ASZ} strain areas shows a progressive rotation of NNE-striking F_3^{ASZ} axial planes towards parallelism with S_3^{ASZ} and a rotation of F_3^{ASZ} fold axes toward the L_3^{ASZ} direction. This is qualitatively shown in the equal area plots in Fig. 7. This rotation of F_3^{ASZ} fold axes is also indicated by the pattern of folded L_2^{ASZ} lineations in intermediate strain zones. By unfolding S_2^{ASZ} surfaces around F_3^{ASZ} hinges following the methods of Ghosh (1993), the resulting curvilinear pattern of L_2^{ASZ} (Fig. 6c) indicates a relative rotation of fold F_3^{ASZ} axes with respect to L_2^{ASZ} directions during D_3^{ASZ}.

4.2. Application of the R_f/ϕ technique

The abundance of deformed pebble-sized feldspar and quartz porphyroclasts in a fine-grained matrix within the Thurso Gneiss (Figs. 4b and 8) and a deformed conglomerate layer (Fig. 4a) provided us with a means of estimating the finite strain state of D_2^{ASZ} and D_3^{ASZ} strain zones within the Anita Shear Zone using the methods described by Lisle (1985), De Paor (1988), and Simpson and De Paor (1993). We aimed to determine the ellipticity and orientation of finite strain by directly measuring the shape (axial ratio, R_f) and axial orientation (ϕ) of deformed feldspar and quartz porphyroclasts in the metapsammite and elliptical cobbles in a deformed conglomerate layer at site 97106 and elsewhere in the shear zone (Fig. 7). Whether or not the values we obtained reflect actual finite strains for the deformations studied depends upon the following assumptions (1) the clasts acted as passive ellipses and deformed homogeneously within their matrix, (2) there was no interaction between clasts during deformation, and (3) the rock did not possess a pre-existing fabric. To ensure no interaction between clasts, we only measured isolated grains. The occurrence of an identical, relatively homogeneous metapsammitic lithology and the same conglomerate layer within *both* low and adjacent high strain zones at site 97106 permitted an uncomplicated comparison of strain data obtained from the different strain domains. A description of statistical methods (I_{sym} and χ^2) to test the other two assumptions are provided by both Lisle (1985) and De Paor (1988) and are discussed in more detail below.

We measured clasts that were distributed uniformly through the rock at three different scales of observation: the outcrop scale (entire width of D_2^{ASZ} and D_3^{ASZ} strain zones in Fig. 7), thin section scale ($45 \times 25\ mm^2$) and sub-thin section scale ($3.5 \times 2\ mm^2$). Measurements of orientation (ϕ) and aspect ratio (R_f) were made on three mutually perpendicular surfaces cut relative to the dominant L–S fabric elements in each domain: (1) perpendicular to

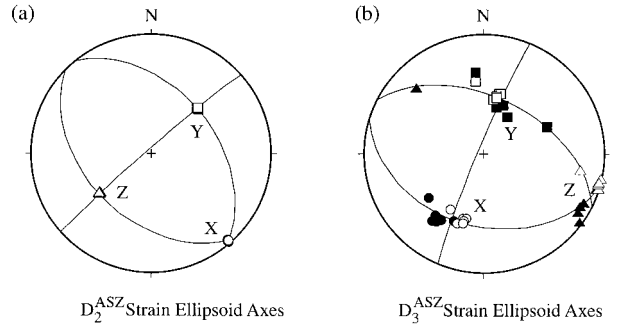

Fig. 9. Lower hemisphere equal-area stereoplots of the best fit finite strain axes and principal planes of strain discussed in the text. (a) Best fit estimates of the strain axes for D_2^{ASZ} (samples from Thurso Gneiss, 97106I). (b) Twelve estimates of the strain axes for D_3^{ASZ} from two samples (Thurso Gneiss, 97106E, black-filled shapes and Milford Gneiss, 97107, white-filled shapes). Listed orientations show plunge and plunge direction of axes.

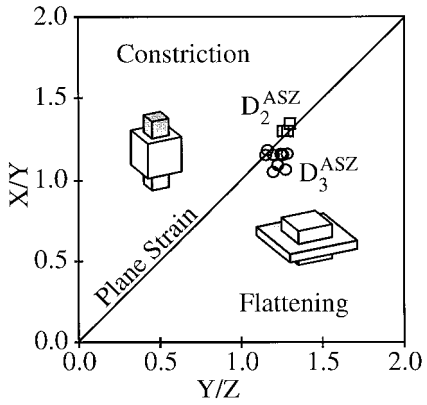

Fig. 10. Flinn plot of D_2^{ASZ} (squares) and D_3^{ASZ} (circles) strain data presented in Table 1.

stretching lineation (*YZ*-plane), (2) parallel to foliation (*XY*-plane), and (3) parallel to stretching lineation and perpendicular to foliation (*XZ*-plane). An average of over 100 individual measurements (>30 per face) were made for each sample collected (Table 1). Best fit curves for each data set were found manually using the methods of Lisle (1985) and De Paor (1988) and were compared with curves determined using the computer software package, R_f/Fry v.2.0.6 (De Paor and Simpson, 1995). All methods applied yielded results in excellent agreement. Following this we calculated the best fit three-dimensional ellipsoid for each sample by recombining the harmonic mean of ellipses found for each of the three perpendicular planes (recommended by Lisle, 1985) according to the least squares method described by Owens (1984).

The best fit three-dimensional strain ellipsoids for D_2^{ASZ} and D_3^{ASZ} strain zones are shown in Fig. 9. Most notably, the orientations of the three principal axes of

Table 2
Representative microprobe analyses (wt% oxide and cation data) of equilibrium assemblages

	D_2^{ASZ}						D_3^{ASZ}					
	Garnet	Amphibole	Plagioclase	Biotite	Rutile	Clinozoisite	Garnet	Amphibole	Plagioclase	Biotite	Titanite	Clinozoisite
SiO_2	37.3	42.9	61.6	37.6	0.0	39.4	37.5	42.4	59.8	36.3	30.5	38.2
TiO_2	0.0	0.5	0.0	1.5	98.9	0.1	0.0	0.4	0.0	2.3	38.8	0.2
Al_2O_3	21.4	16.7	24.1	17.9	0.0	32.4	21.4	14.7	24.7	17.8	1.3	28.9
Cr_2O_3	0.0	0.0	0.0	0.0	0.2	0.0	0.1	0.1	0.0	0.0	0.0	0.1
FeO	28.8	14.1	0.0	16.5	0.1	1.3	24.1	16.4	0.1	17.1	0.3	5.2
MnO	0.6	0.1	0.0	0.0	0.0	0.0	2.5	0.2	0.0	0.1	0.1	0.0
MgO	3.6	9.8	0.0	11.9	0.0	0.0	2.2	8.5	0.0	10.4	0.0	0.0
CaO	7.2	11.0	5.5	0.1	0.1	24.3	11.6	11.6	6.6	0.0	28.3	23.4
Na_2O	0.0	1.6	8.6	0.2	0.0	0.0	0.0	1.4	7.9	0.1	0.0	0.0
K_2O	0.0	0.5	0.1	8.9	0.0	0.0	0.0	0.9	0.1	9.4	0.0	0.0
Total	99.0	97.1	99.9	94.6	99.4	97.5	99.5	96.7	99.2	93.4	99.2	96.1
# oxygens	12	23	8	22	2	26	12	23	8	22	5	26
Si	3.0	6.3	2.7	5.6	0.0	6.0	3.0	6.4	2.7	5.6	1.0	6.3
Ti	0.0	0.1	0.0	0.2	1.0	0.0	0.0	0.0	0.0	0.3	1.0	0.0
Al	2.0	2.9	1.3	3.2	0.0	5.8	2.0	2.6	1.3	3.2	0.0	5.6
Cr	0.0	0.0	0.0	0.0	0.0	0.0	0.0	0.0	0.0	0.0	0.0	0.0
Fe	1.9	1.7	0.0	2.1	0.0	0.2	1.6	2.1	0.0	2.2	0.0	0.7
Mn	0.0	0.0	0.0	0.0	0.0	0.0	0.2	0.0	0.0	0.0	0.0	0.0
Mg	0.4	2.2	0.0	2.7	0.0	0.0	0.3	1.9	0.0	2.4	0.0	0.0
Ca	0.6	1.7	0.3	0.0	0.0	4.0	1.0	1.9	0.3	0.0	1.0	4.1
Na	0.0	0.5	0.7	0.1	0.0	0.0	0.0	0.4	0.7	0.0	0.0	0.0
K	0.0	0.1	0.0	1.7	0.0	0.0	0.0	0.2	0.0	1.8	0.0	0.0
Total	8.0	15.5	5.0	15.5	1.0	16.0	8.0	15.5	5.0	15.5	3.0	16.8
	$T = 581 \pm 34$°C, $P = 11.9 \pm 1.12$ kbar						$T = 587 \pm 42$°C, $P = 8.7 \pm 1.24$ kbar					

the finite strain ellipsoid (X, Y, Z) for D_2^{ASZ} strain zones of the shear zone are oriented at high angles to the axes of strain in D_3^{ASZ} strain zones (Fig. 9). The X-axis for D_2^{ASZ} is 70° from the X-axis for D_3^{ASZ}; the Y-axis for D_2^{ASZ} is 20° from the Y-axis for D_3^{ASZ}; and the Z-axis for D_2^{ASZ} is 107° from the Z-axis for D_3^{ASZ} (other angles include 26° between the X-axis for D_2^{ASZ} and the Z-axis for D_3^{ASZ}; and 19.5° between the Z-axis for D_2^{ASZ} and the X-axis for D_3^{ASZ}). These results also indicate that the L_2^{ASZ} and L_3^{ASZ} stretching lineations parallel the X-axes of the strain ellipsoids in each domain, respectively (compare Fig. 9 with Fig. 7). In addition, the XY-plane of finite strain in D_3^{ASZ} strain zones parallels S_3^{ASZ} and the boundaries of the shear zone, and the XY-plane of finite strain in D_2^{ASZ} strain domains parallels S_2^{ASZ}, nearly orthogonal to XY in adjacent D_3^{ASZ} strain zones. For D_3^{ASZ} strain zones, the XY-plane also parallels the NNE-trending subvertical boundaries of the shear zone itself (compare XY-plane in Fig. 10 with Fig. 3d). In addition to orientation, the results of our strain analyses are consistent with deformation in both D_2^{ASZ} and D_3^{ASZ} strain domains deviating only slightly from plane strain (Fig. 10) assuming minimal volume loss. The slight deviations from plane strain suggest that D_2^{ASZ} involved slightly more constrictional strains and D_3^{ASZ} plus D_2^{ASZ} in high strain zones represents slightly more flattening strains (Fig. 10).

The assumption of volume loss during deformation within the shear zone is difficult to assess, especially during D_2^{ASZ}. There is no geological evidence in the form of veins, intrusions, pegmatites or other features that suggest a significant volume of material was added during deformation. Microprobe analyses (Table 2) show changes in mineral chemistry (major elements) within the rims of some matrix minerals. These data suggest that some local volume or area change by the diffusion of mobile elements within the matrix occurred during D_3^{ASZ}. However, because our measurements of strain were made at both the thin section and outcrop scales and both studies yielded similar results, we suggest that the scale at which we measured strain greatly exceeded the length scale of diffusion within the shear zone. In addition, across strain domains and in similar lithologies, the mineralogy of samples, grain sizes, and the modal abundance of mineral phases are virtually identical. The only significant phase changes involved the growth of titanite and loss of rutile during D_3^{ASZ}, and the modal abundances of these minerals are very small (less than 0.5% area). Despite these observations, however, volume loss during deformation is possible and, hence, could affect our evaluation of plane strain. Nevertheless, the clast–matrix relationships we employed in our kinematic vorticity studies, discussed below, provide an independent means of justifying the condition of plane strain.

Statistical methods to test the assumptions of homogeneous behavior (χ^2) and initial distribution of clasts (I_{sym}) are presented by Lisle (1985) and De Paor (1988). In all of our analyses, the data sets passed these statistical tests (Table 1). A comparison of the two different methods of analysis described by Lisle (1985) and De Paor (1988) suggest that analytical errors are low (± 0.03; compare values obtained in both methods in Table 1). Despite passing these tests, the microstructures of the samples analyzed strongly suggest a significant deviation from passive behavior. An abundance of asymmetric recrystallized tails on the feldspar porphyroclasts (not included in measurement of clast aspect ratio) and a deflection of foliation around the clasts indicates that the clasts behaved as nearly rigid objects during non-coaxial flow. This mechanical behavior is ideally suited for our kinematic vorticity analyses (described below) but less well suited for finite strain studies, leading to an underestimation of the magnitude of strain. Rigid rotation during deformation rather than passive shape change explains why the R_s values obtained for the L_2^{ASZ}–S_2^{ASZ} and L_3^{ASZ}–S_3^{ASZ} fabrics and the axial ratios of the clasts are similar Table 1. The data suggest that although the behavior of the clasts deviates from ideal passive behavior, this behavior is the same for both strain zones studied. We therefore judge these data to be useful in evaluating and comparing the behavior of clasts during D_2^{ASZ} and D_3^{ASZ}, evaluating the possibility of plane strain, and identifying differences in the orientation of the principal axes of finite strain in each domain. We also tested our results from site 97106 using a variety of different lithologies including the conglomerate layer, mafic enclaves, and feldspar aggregates in the mafic Milford Gneiss. The results are all in good agreement (e.g. Table 1) and are not scale-dependent suggesting that our data reflect real similarities and differences between domains.

The possible effects of pre-existing fabrics in the D_3^{ASZ} strain domain are difficult to discern using statistical tests. Although all of our analyses passed the I_{sym} test, we initially had expected low I_{sym} values (below acceptable values of 0.51) in the YZ-plane of D_3^{ASZ} strain which coincides with the XZ-plane of D_2^{ASZ} strain. Possible explanations for the absence of low values include the following: symmetrical R_f/ϕ patterns can result from either coaxial straining of a pre-existing symmetric fabric or the oblique straining of an asymmetric one (Lisle, 1985). Because, as we show later, D_3^{ASZ} was dominated by pure shear applied at a high angle to the L_2^{ASZ}–S_2^{ASZ} fabric, the initial preferred orientation of clasts produced by D_2^{ASZ} deformation may not have produced a discernible effect given current methods of analysis. In addition, if clast

reorientation rather than shape change was the dominant process affecting the clasts during deformation, as the similar clast axial ratios and R_s values we obtained suggest, our measurements may not discern the full effects of a pre-existing shape fabric.

5. Kinematic and vorticity analyses

In this section we use systems of rotated porphyroclasts and asymmetric microstructures from localities at Poison Bay, including site 97106 (Fig. 7), to compare the kinematics of ductile flow that produced the L_2^{ASZ}–S_2^{ASZ} and L_3^{ASZ}–S_3^{ASZ} fabrics. Our aim was to (1) determine the senses and directions of displacement associated with each fabric; (2) determine the deformation type and kinematic vorticity number (W_k) of the flow regime that produced the L_2^{ASZ}–S_2^{ASZ} and L_3^{ASZ}–S_3^{ASZ} fabrics to establish whether they are similar or different; and (3) assess whether these deformations are consistent with transpression, transtension, contraction, or extension, etc. The methods we apply to achieve the first two tasks are well established and have been described in detail by others (e.g. Passchier, 1987; Simpson and De Paor, 1993; Wallis, 1995). Below we briefly summarize our application of this analysis followed by a description of the microstructure and porphyroclast systems in the samples we have used. Lastly we evaluate the results of our analysis.

In the study of ductile shear zones, the simplifying assumption of a system dominated by simple shear is often made despite the possibility of many other types of deformation. In plane strain deformation, for example, general non-coaxial deformation can be any combination of simple shear and pure shear components (Lister and Williams, 1983; Passchier, 1986). Passchier (1987; Passchier and Urai, 1988) defined the kinematic vorticity number (W_k) as a useful means of describing the degree of non-coaxiality in a shear zone where $W_k = 0$ is pure shear and $W_k = 1$ is simple shear. Within a general non-coaxial flow field undergoing plane strain, two lines, called eigenvectors, define directions of no rotation. For a contracting shear zone (sub-simple shear), one eigenvector usually is fixed to the flow plane of the simple shear component of deformation (Simpson and De Paor, 1993). The orientation of the other non-rotating line is dependent on the relative magnitude of the pure and simple shear components. Hence, by determining the orientation of both these stable eigenvectors in a steady flow field, the kinematic vorticity of flow can be determined by measuring the angle (ν) between them (Bobyarchick, 1986; Simpson and De Paor, 1993).

$$W_k = \cos(\nu) \quad (1)$$

For reference, the angle between the two eigenvectors is 90° for wholly pure shear and 0° for wholly simple shear, but an angle of 45° does not mean equal components of simple and pure shear. We discuss this nonlinear relationship in context with our results below.

Measurement of three-dimensional kinematic vorticity in naturally deformed rocks is complicated by a number of unsolved problems (Tikoff and Fossen, 1995). Nevertheless, we suggest that a two-dimensional analysis of vorticity within the XZ-plane is effective and justifiable in our case because of evidence of plane strain during D_2^{ASZ} and D_3^{ASZ}. Evidence for plane strain includes the results of our finite strain study (Fig. 10) and an analysis of clast–matrix relationships in the rocks studied. For example, deviations from plane strain could potentially involve the loss or gain of area out of the XZ-plane (plane of observation) by the extrusion of clast or matrix material in the Y-direction during deformation. However, if lateral extrusion of clast material occurred, this effect should be discernable in changes in the distribution of clast sizes and shapes measured in different strain domains in our finite strain study (Srivastava et al., 1995). The low R_s values we obtained and evidence of dominantly rigid clast behavior during deformation suggests that movement of clast material out of the XZ-plane did not occur during D_2^{ASZ} and D_3^{ASZ}. Lateral extrusion of matrix material parallel to Y during deformation is also not supported by the monoclinic symmetry of matrix tails on the feldspar clasts used in our kinematic vorticity study (microstructure presented below). Finally, another possible deviation from plane strain could have occurred if a large number of clasts rotated in planes other than the XZ-plane. However, we only observed asymmetric tails in the XZ-plane suggesting that clast rotation occurred mainly within the XZ-plane for each episode of deformation.

A measure of the orientation and aspect ratios of rigid porphyroclasts rotating in a homogeneously deforming ductile matrix can provide an estimate of both strain path and W_k (e.g. Passchier, 1987; Simpson and De Paor, 1993; Wallis, 1995). The basis for this method is the theoretical work of Jeffrey (1923), Ghosh and Ramberg (1976), Freeman (1985) and Passchier (1987) which describes the motion of rigid ellipsoidal particles in a steady non-coaxial flow field. Rigid porphyroclast systems displaying asymmetric recrystallized tails in mylonites are extremely useful for determining shear sense (Simpson and Schmid, 1983) and are also indicators of incremental strains, ductile flow, and finite strain. Using these systems in kinematic vorticity studies relies on the recognition of microstructures that reveal the rotation history of the clasts. The correct identification of clasts that have rotated forward vs those that have rotated backward and those in their stable end orientations is

critical for determining the orientation of the eigenvectors of flow. A wide range of clast shapes and orientations are needed. The eigenvector that is inclined relative to the flow plane separates fields of back-rotating vs forward-rotating grains (Simpson and De Paor, 1993). Backward-rotated objects are generally possible in homogeneous flow regimes only if there is a significant deviation from simple shear and the rotating objects are rigid and more elongate than some critical value (Simpson and De Paor, 1993; Wallis, 1995).

5.1. Microstructure and sense of shear indicators

In this subsection we describe the microstructures that we used in determining W_k for D_2^{ASZ} and D_3^{ASZ} strains at Poison Bay and justify the assumptions involved in this analysis. One advantage of using site 97106 is that here we were able to compare measurements made within the exact same lithology (metapsammite) and using similar clast–matrix grain size ratios in different strain domains. The metamorphic mineral assemblages that define each of the two foliations studied differ primarily in some aspects of their mineral chemistry and the occurrence of minor minerals such as rutile and titanite and not in major phases. These differences, while extremely useful in our metamorphic study, do not appear to have affected the microstructure of the deformed porphyroclasts systems we used.

All samples used were collected from zones that contain well defined planar and linear fabric elements. The matrix of the samples analyzed at site 97106 is composed of fine-grained (10–15 microns) quartz + feldspar ± mica with minor amphibole + clinozoisite + garnet grains uniformly distributed throughout the rock. This unit contains large coarse-grained (from 3 mm to >10 mm) feldspar clasts that are also uniformly distributed throughout the rock (Fig. 8). Most of these coarse clasts are not touching other clasts (Fig. 8). The feldspar clasts display a wide range of aspect ratios and orientations which have helped us to determine accurately the orientation of the eigenvectors of flow in both fabrics studied. The feldspar clasts display dynamically recrystallized tails composed of fine-grained matrix material and a thin (a few microns maximum) recrystallized rim surrounding a central core that exhibited no evidence of dynamic recrystallization and limited disruption of crystal lattices. The recrystallized tails define a well developed stretching lineation strung out within foliation planes. The cores are homogeneous in texture and composition, whereas rims exhibit a slightly different mineral chemistry. Rigid behavior of the clast cores during non-coaxial flow is indicated by deflection of foliation around the clasts and the development of asymmetric tails in both strain domains. In addition, the foliation

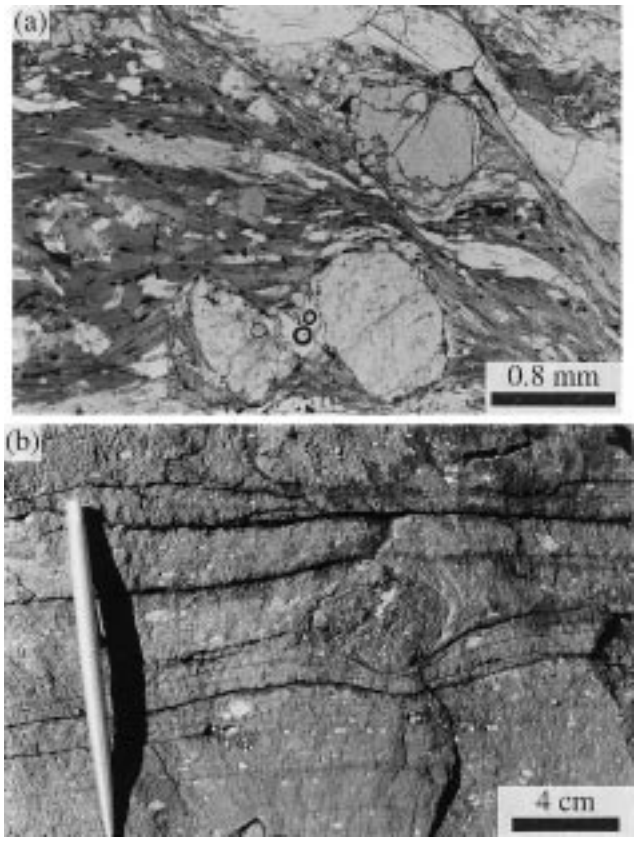

Fig. 11. (a) Thin section view (plane light) of a microfaulted feldspar clast and C' shear band cleavage indicating a dextral sense of shear during D_3^{ASZ} at Poison Bay. Sample is from the Saint Anne Gneiss. (b) View of a vertical outcrop face showing δ-type recrystallized tails on a mafic clast showing top-down-to-the-SSE (to the right) dextral sense of shear during D_2^{ASZ} in a psammite layer of the Thurso Gneiss at Poison Bay.

does not change character near the tails and no boudinage of the tail material was observed, suggesting that the tails approached passive behavior during deformation.

A wide array of both σ-type, δ-type, and complex σ–δ-type systems indicating both sinistral and dextral senses of shear were observed in the XZ-planes of both strain domains (e.g. Fig. 8b). Few asymmetric structures were observed in the XY- and YZ-planes, in accordance with plane strain. A statistical analysis of over 300 grains for D_2^{ASZ} and over 200 grains for D_3^{ASZ} (n, Table 1) shows that the dextral shear sense was dominant for both deformation events. This shear sense defines the sense of forward rotation (dextral) for each strain domain. D_2^{ASZ}, however, involved top-down-to-the-SE transport whereas D_3^{ASZ} involved subhorizontal, NNE–SSW dextral displacements nearly orthogonal to L_2^{ASZ}. In addition to asymmetric tails on feldspar clasts, numerous other kinematic indicators are present in both D_2^{ASZ} and D_3^{ASZ} strain domains. These include C' shear bands, fractured and microfaulted feldspar grains (Fig. 11a), macroscopic δ-tails

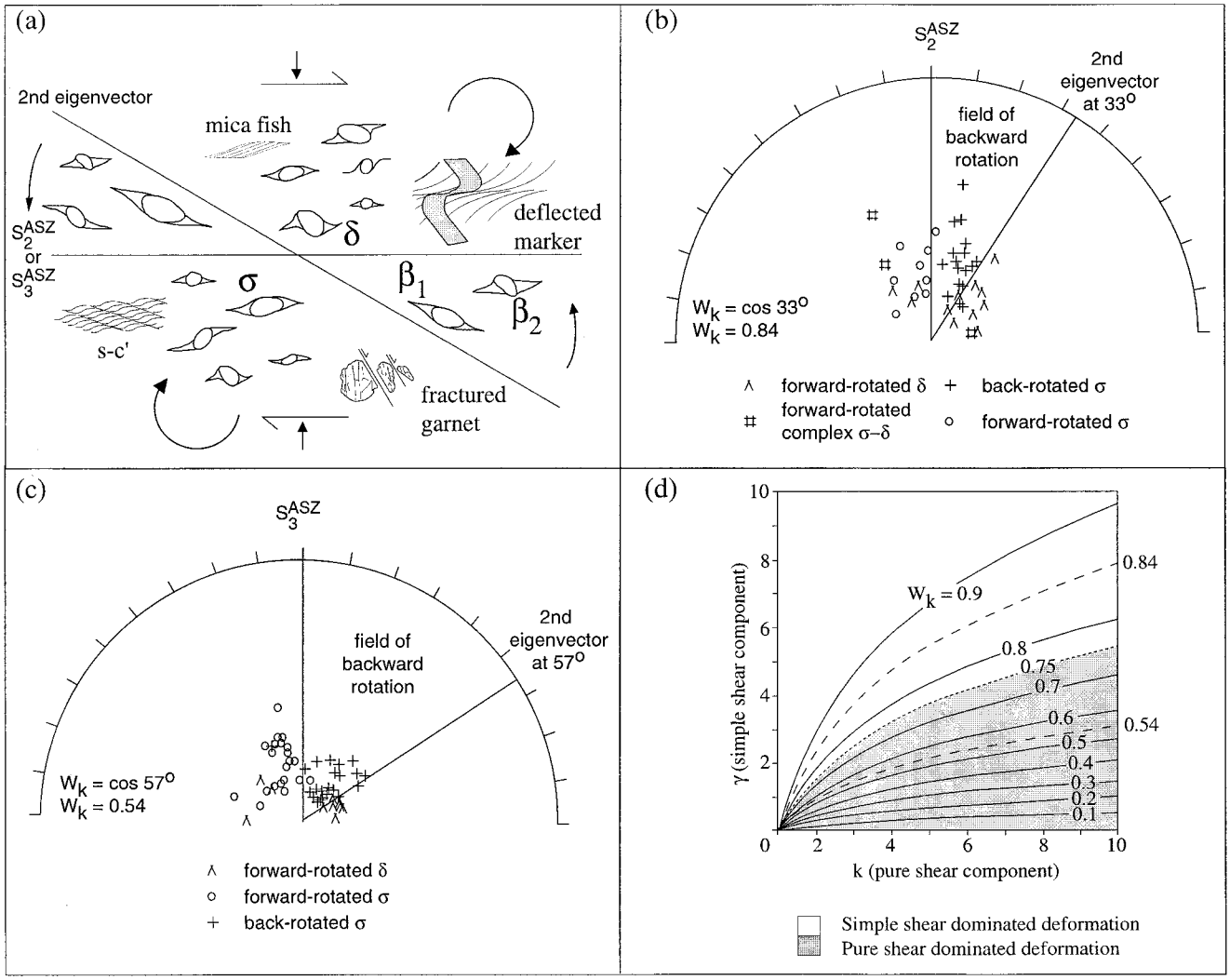

Fig. 12. (a) Compiled sketch of microstructures used to define fields of forward and backward rotation in deformed samples at Poison Bay. Traces of S_2^{ASZ} and S_3^{ASZ} are horizontal. (b), (c) Plots of kinematic vorticity data on a hyperbolic net for D_2^{ASZ} and D_3^{ASZ}, respectively. Stable eigenvectors are shown as lines. See Simpson and De Paor (1993) and De Paor (1988) for plotting procedure. (d) Plot showing paths of constant W_k in γ–k space for plane strain combinations of simultaneous pure and simple shearing. Non-linearity of W_k paths is a result of the finite strain caused by the pure shear component increasing faster than that caused by the simple shear component (taken from Tikoff and Fossen, 1995). See text for discussion.

on large mafic clasts (Fig. 11b), mica fish, and minor shear zones that parallel the main foliation in each domain.

In all of the clasts studied in the *XZ*-plane of observation, the following patterns were observed (Fig. 12a): In each domain, clasts with δ-tails were consistently oriented at high angles to foliation ($>30°$ in D_2^{ASZ} domain; $>50°$ in D_3^{ASZ} domain). These types of tails usually form in very high strain or ultramylonite zones (Passchier, 1987) and are indicators of continuous forward rotation. Clasts oriented at low angles to foliation, displayed σ-tails indicating either sinistral or dextral sense of shear. Dextral σ-tails formed on the narrow ends of grains were always inclined upstream (dip-direction points upstream). These clasts were by far the dominant type and are interpreted as forward-rotated clasts. Two types of backward-rotated clasts were recognized by the following criteria: (1) following Passchier (1987) and Simpson and De Paor (1993), clasts inclined downstream with dextral σ-tails attached to broad sides of the clasts (β_2, Fig. 8b and 12a); and (2) clasts inclined upstream or downstream that displayed sinistral σ-tails either to broad side or narrow ends (β_1, Figs. 8b and 12a). Those grains inclined downstream with sinistral tails on their narrow ends are probably near their stable orientations (Passchier, 1987). Together these patterns defined three main fields within the *XZ*-plane of each domain: A field of forward-rotated dextral σ grains, a field of forward-rotated dextral δ grains, and a field of backward-

rotated σ grains showing either sinistral shear senses or a downstream inclination (Fig. 12a).

5.2. Kinematic vorticity analysis

We collected R_f/ϕ data from three samples from the XZ-plane of finite strain in the D_3^{ASZ} and D_2^{ASZ} strain domains. The reference frame we use is with respect to the axes of finite strain in these strain domains, respectively. A two-dimensional analysis is justified by the results of our finite strain and microstructural analyses, both of which suggest approximate plane strain conditions for both deformation events. In each sample over 40 grains were measured (a minimum of 16 required according to De Paor, 1988) and distinguished on the basis of rotation sense and type of asymmetric tail (defined in previous section). A wide range in grain shape and orientation was used including relatively equant to highly elongate grains. Thin sections were cut thicker than normal to reveal the orientation in the third dimension, and individuals that were cut obliquely or impinged on their neighbors were rejected. Four categories of grains were measured: (1) forward-rotated δ grains, (2) forward-rotated complex σ–δ grains, (3) backward-rotated σ grains, (4) forward-rotated σ grains. We then plotted these data on a hyperbolic orientation net using different symbols (Fig. 12b, c) for each category (plotting methods described by De Paor, 1988; Simpson and De Paor, 1993). We take the foliation trace to be sub-parallel to the shear zone boundary in each domain. This is well justified on the basis of the following (1) S_3^{ASZ} parallels the shear zone boundaries, (2) finite strain data indicate that the XZ-plane parallels the main foliation in each domain, and (3) each domain contains mylonites or, in the case of D_2^{ASZ}, ultramylonites resulting from high strains. One stable eigenvector parallels the shear zone boundaries (Simpson and De Paor, 1993). The second eigenvector, together with the shear zone boundary, encloses the field of backward-rotated grains on a hyperbolic net containing our porphyroclast data (Fig. 12b, c; De Paor, 1988; Simpson and De Paor, 1993). The cosine of the angle between the two eigenvectors yielded our estimate of W_k [Eq. (1)].

The results of our analysis indicate that for D_2^{ASZ}, $W_k = 0.84$ and for D_3^{ASZ}, $W_k = 0.54$ (Fig. 12b, c). Both shear zones are narrowing shear zones. The results define a good spread of clast orientations (perimeter of net) and axial ratios (radius of net), enabling us to accurately define the locations of the eigenvector separating the fields of backward and forward rotation. Because of the excellent spread of data, we were able to estimate the degree of error in the location of the eigenvectors as less than 2°. This translates into an error in W_k as ± 0.05. Values of W_k in the range 0–0.75 indicate pure-shear dominated deformation whereas values of W_k in the range 0.75–1 indicate that deformation was dominated by simple shear (Fig. 12d). This inequality is known as the 'pure shear bias' of W_k (Tikoff and Fossen, 1995). Our results therefore indicate that D_2^{ASZ} was dominated by dextral, top-down-to-the-SE simple shear. In contrast, D_3^{ASZ} was dominated by pure shear involving a strong component of horizontal shortening perpendicular to the shear zone boundaries and a dextral simple shear component resulting in NNE–SSW subhorizontal displacements.

6. Conditions of metamorphism during D_2^{ASZ} and D_3^{ASZ}

Metapelitic mineral assemblages of garnet, plagioclase, clinozoisite, biotite, and calcic amphibole define the L_2^{ASZ}–S_2^{ASZ} and L_3^{ASZ}–S_3^{ASZ} fabrics in different strain domains within the Anita Shear Zone. Only the growth of titanite and absence of rutile from D_3^{ASZ} domains represent phase changes between the two strain domains. Titanite is absent in the L_2^{ASZ}–S_2^{ASZ} assemblage. We have selected samples from nearly identical metapelitic protoliths from each strain domain to calculate and compare the pressure (P) and temperature (T) conditions of metamorphism that accompanied the development of L_2^{ASZ}–S_2^{ASZ} and L_3^{ASZ}–S_3^{ASZ} within the shear zone. The basis for these calculations is that, despite a similar overall assemblage, the chemistry of the constituent minerals in each domain is quantifiably different. These differences in chemistry, combined with textural relationships, allowed us to calculate and compare the P–T conditions of metamorphism that accompanied the D_2^{ASZ} and D_3^{ASZ} deformation events. The results show that D_2^{ASZ} and D_3^{ASZ} occurred at different crustal levels.

Several observations suggest that the conditions of metamorphism we have determined occurred during deformation for the two events studied. Firstly, the minerals in the assemblages we have used in our calculations define the L_2^{ASZ}–S_2^{ASZ} and L_3^{ASZ}–S_3^{ASZ} structural elements in each strain domain. Secondly, textural relationships suggest syntectonic mineral growth. Within D_2^{ASZ} strain domains, for example, spiral and curved inclusion trails within garnet grains are consistent with syntectonic porphyroblast growth. Thirdly, the relative timing of mineral growth in the D_2^{ASZ} and D_3^{ASZ} domains, respectively, is very well constrained. Titanite, for example, defines S_3^{ASZ} but does not form part of the mineral assemblages that define S_2^{ASZ} in identical lithologies, indicating syn-D_3^{ASZ} mineral growth. Microprobe data and mineral X-ray maps also indicate that the two strain domains display different compositions of syntectonic garnet growth. Garnet

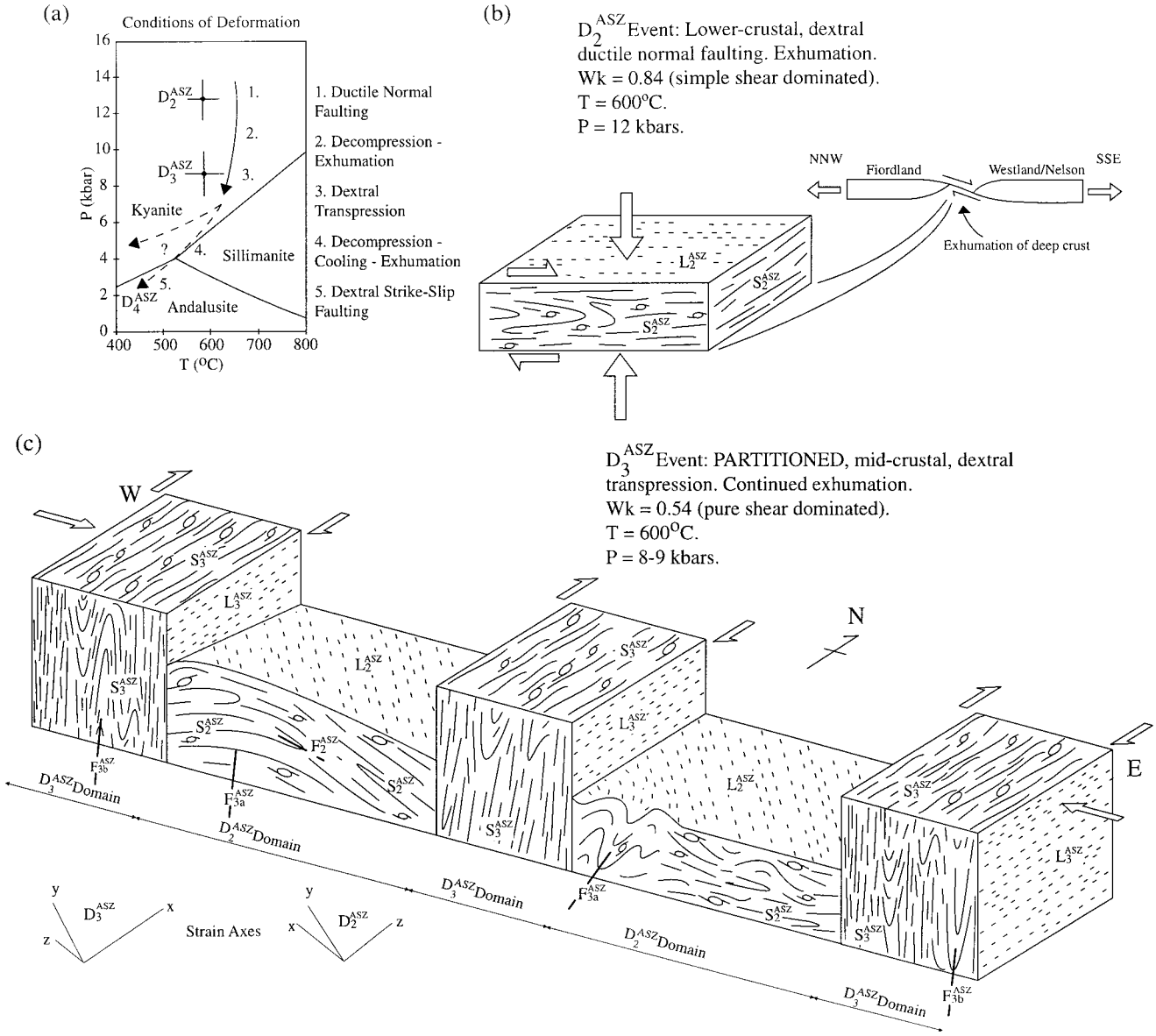

Fig. 13. (a) Diagram showing *P–T* path and accompanying changes in style and type of deformation in the Anita Shear Zone. The crosses mark the final results of our Thermobarometric estimations using THERMOCALC v.2.6. The length of the lines of the cross represent 2σ error bars. See text for discussion. (b) Summary cartoon of D_2^{ASZ} deformation showing interpretation of ductile normal faulting and lower crustal thinning. (c) Cartoon showing geometry of dextral transpressional D_3^{ASZ} deformation superimposed on D_2^{ASZ} structures. Strain domains and a three-dimensional rendering of strain axes are shown for comparison.

that occurs within D_2^{ASZ} domains is homogeneous. In contrast, in D_3^{ASZ} domains, chemically distinct garnet forms overgrowths on garnet cores that have compositions identical to garnet in the D_2^{ASZ} domains. The garnet overgrowths have lower Fe and Mg, and higher Ca contents in comparison with garnet cores and garnet that forms part of the L_2^{ASZ}–S_2^{ASZ} assemblages. There are also small garnet grains in the matrix of D_3^{ASZ} domains that have compositions identical to the overgrowths. Plagioclase is slightly more calcic and amphibole is slightly more Fe-rich in D_3^{ASZ} domains than equivalent minerals in D_2^{ASZ} domains (Table 2).

To constrain the *P–T* conditions that accompanied the development of the L_2^{ASZ}–S_2^{ASZ} and L_3^{ASZ}–S_3^{ASZ} assemblages, chemical analyses were obtained using a Cameca SX50 microprobe housed at the University of New South Wales running at an accelerating voltage of 15 kV and a beam width of 1–5 μm (representative analyses from minerals defining the L_2^{ASZ}–S_2^{ASZ} and L_3^{ASZ}–S_3^{ASZ} fabrics shown in Table 2). We employed the method of Powell and Holland (1988, 1994) which involves the determination of the activities of mineral endmembers as described by Holland (1993). The conditions of formation of the mineral assemblages defin-

ing L_2^{ASZ}–S_2^{ASZ} and L_3^{ASZ}–S_3^{ASZ} were determined using microprobe analyses together with average P–T calculations via the computer software THERMOCALC (version 2.6; Powell and Holland, 1988). We used the internally consistent thermodynamic data set of Holland and Powell (1990; data file created April 1996). In finding an average P–T of the mineral assemblages, these methods involve the use of an independent set of reactions between the endmembers of the minerals in the assemblage. Different sets of independent reactions that define a series of P–T lines may be found under different conditions, and the software selects the appropriate set to minimize errors on the calculated P and T conditions. All mineral endmember activities were calculated using the computer program AX (AX shareware written by T.J.B. Holland, http://www.esc.cam.ac.uk/software.html) and the defaults suggested in Powell and Holland (1988). Error bars (2σ length) are shown on the average P and average T calculations (assuming $a_{H_2O} = 1.0$) in Fig. 13(a).

The best fit result suggests that the L_2^{ASZ}–S_2^{ASZ} assemblage equilibrated at 11.9 ± 1.1 kbar and 581 ± 34°C and the L_3^{ASZ}–S_3^{ASZ} assemblage equilibrated at 8.7 ± 1.2 kbar and 587 ± 42°C (Fig. 13a). To test the sensitivity of these results to variations in water activity, results were calculated for $a_{H_2O} = 1.0$–0.4. Decreasing a_{H_2O} only lowered P and T values for both events by approximately 1 kbar and 50°C, respectively, suggesting that our results are robust. The validity of these P–T results was confirmed using completely different protoliths (e.g. garnet-bearing mafic dikes in the Saint Anne Gneiss) that yielded identical results. These results indicate that D_2^{ASZ} occurred in the lower crust at ~40 km depth and D_3^{ASZ} occurred at mid-crustal levels at ~30 km depth. This indicates that D_2^{ASZ} resulted in decompression and rapid, near isothermal exhumation of lower crustal rocks by ~10 km before the onset of D_3^{ASZ}.

7. Discussion

The results of our structural, metamorphic, finite strain and kinematic vorticity analyses show that the Anita Shear Zone resulted from two different types of amphibolite facies mylonitic deformation. These two events (D_2^{ASZ} and D_3^{ASZ}) occurred at different crustal levels and display different geometries and kinematics. In this section we discuss the possible significance of the mylonitic foliations of the Anita Shear Zone by placing the structural and metamorphic characteristics of their development within a regional tectonic framework. Our results also allow us to address the following: (1) the effects of mid-Cretaceous extension and continental rifting on the evolution of northern Fiordland; (2) mechanisms by which lower crustal rocks in northern Fiordland were exhumed; (3) the spatial and kinematic relationships between the subvertical mylonites of the Anita Shear Zone and late Tertiary brittle strike-slip faulting associated with the Alpine fault; and (4) the possible effects of dextral transpression on exhumation of the high P–T rocks in northern Fiordland.

7.1. Significance of D_2^{ASZ}

The results of our structural and kinematic studies of areas in the Anita Shear Zone that were minimally affected by D_3^{ASZ} strain indicate that the L_2^{ASZ}–S_2^{ASZ} fabric formed within a thinning ($W_k = 0.84$), simple shear-dominated shear zone involving top-down-to-the-SE normal displacements. We have attempted to minimize the uncertainties surrounding the possible initial orientations of the Anita Shear Zone during D_2^{ASZ} by (1) objectively defining variations in strain within the shear zone; (2) documenting the effects of F_3^{ASZ} on L_2^{ASZ}–S_2^{ASZ} orientations; and (3) showing that minimal reorientation of L_2^{ASZ}–S_2^{ASZ} by younger F_3^{ASZ} folding occurs within D_2^{ASZ} domains. These relationships and the consistent subhorizontal orientation of S_2^{ASZ} in D_2^{ASZ} domains across the shear zone strongly suggests that these domains preserve the approximate original geometry of L_2^{ASZ}–S_2^{ASZ}. Even if some reorientation occurred, we emphasize that such rotations would not effect the results of our kinematic vorticity analysis nor our metamorphic results (discussed below) but would only tend to change the direction of D_2^{ASZ} transport (L_2^{ASZ}).

P–T estimates using metamorphic mineral assemblages that define L_2^{ASZ}–S_2^{ASZ} indicate that D_2^{ASZ} displacements and crustal thinning in the Anita Shear Zone occurred under lower crustal conditions at depths of ~40 km. These depths, compared with the ~30 km depth of D_3^{ASZ} deformation, indicate that the lower crustal rocks affected by D_2^{ASZ} experienced decompression and exhumation to mid-crustal levels by the removal of ~10 km of crust prior to the onset of D_3^{ASZ} (Fig. 13a). These data, together with our structural and kinematic data are consistent with the Anita Shear Zone having initially formed as a major ductile normal fault that led to thinning of the lower crust and the tectonic unroofing of lower crustal granulites (Fig. 13a, b). The removal of overlying crust through normal displacement within a thinning, gently dipping shear zone explains how these lower crustal granulites were exhumed to mid-crustal levels prior to D_3^{ASZ}.

The approximate age of ductile normal faulting in the Anita Shear Zone is constrained by several relationships. Firstly, L_2^{ASZ}–S_2^{ASZ} (and L_3^{ASZ}–S_3^{ASZ}) at Poison Bay deforms plutonic rocks of the Western

Fiordland Orthogneiss that has been dated at ~126–119 Ma (Mattinson et al., 1986; Bradshaw, 1989). Secondly, S_2^{ASZ} of the Anita Shear Zone is very similar in style, orientation and sequence of formation with respect to the Western Fiordland Orthogneiss as the foliation that forms the Doubtful Sound Shear Zone in central Fiordland. This latter shear zone, which also deforms granulite facies rocks of the Western Fiordland Orthogneiss, has been interpreted as a gently dipping ductile normal fault that influenced the exhumation of lower crustal rocks in the mid-Cretaceous (Gibson et al., 1988; Gibson and Ireland, 1995). Stretching directions in the Anita Shear zone, however, plunge to the NNW, whereas those in the Doubtful Sound Shear Zone are oriented NE. Nevertheless, in light of these relationships, we suggest that D_2^{ASZ} occurred simultaneously with or after mid-Cretaceous continental extension and ductile normal faulting in central Fiordland (Gibson et al., 1988; Gibson and Ireland, 1995). Exhumation of lower crustal rocks by ductile normal faulting in the Anita Shear Zone at this time is also compatible with evidence for upper crustal normal faulting beginning at ~108 Ma in the Paparoa core complex of the Nelson–Westland region (Tulloch and Kimbrough, 1989).

Our final interpretation of a mid-Cretaceous or younger age for initial development of the Anita Shear Zone and correlation of our D_2^{ASZ} deformation with the Doubtful Sound Shear Zone resembles hypotheses first proposed by Hill (1995b). However, Hill (1995a, b) suggested that the subvertical foliation of the shear zone (our L_3^{ASZ}–S_3^{ASZ} fabric) formed during regional Cretaceous ductile normal faulting which we interpret as reflecting dextral transpression.

7.2. Significance of D_3^{ASZ} and D_4^{ASZ}

Structural, kinematic vorticity, metamorphic, and strain data show that the D_3^{ASZ} event in the Anita Shear Zone differed from D_2^{ASZ} in kinematic development, orientation, metamorphic conditions and type of deformation (Fig. 13a, c). Our data indicate that D_3^{ASZ} constitutes a major pure-shear dominated ($W_k = 0.54$) dextral transpressional event (Fig. 13c) that produced the dominant L_3^{ASZ}–S_3^{ASZ} fabric in the Anita Shear Zone. Supporting our kinematic vorticity study, an analysis of F_3^{ASZ} shows that a large degree of subhorizontal shortening (>70% in some areas) occurred perpendicular to the shear zone boundaries during D_3^{ASZ}. The progressive development of S_3^{ASZ} parallel to the axial planes of F_3^{ASZ} folds also indicates that S_3^{ASZ} formed in a subvertical orientation at mid-crustal levels simultaneously with F_3^{ASZ} folding. These results support interpretations that the steep L_3^{ASZ}–S_3^{ASZ} fabric reflects dextral transpressional deformation.

Recognition of a major 4-km-wide, post-mid-Cretaceous dextral transpressional shear zone in northern Fiordland raises important new possibilities for the late Mesozoic–Cenozoic tectonic evolution of northern Fiordland. One possible interpretation is that D_3^{ASZ} reflects a response to an early Tertiary reorganization of the Australian–Pacific plate boundary, possibly including the cessation of seafloor spreading along the Tasman mid-ocean ridge at ~52–47 Ma (Lawver and Gahagan, 1994). The D_3^{ASZ} event could also have resulted from latest Cretaceous or early Tertiary oblique convergence between two or more of the numerous microplates or crustal fragments that characterized this region during the last stages of the opening of the Tasman Sea (Gaina et al., 1998). Interestingly, our data suggest that parts of northern Fiordland were still at mid-crustal levels following the D_2^{ASZ} extensional event. A careful isotopic analysis of the titanites that define the L_3^{ASZ}–S_3^{ASZ} fabric will help determine the exact age and cause of D_3^{ASZ} (Klepeis and Daczko, in preparation). D_4^{ASZ} appears to represent a late Tertiary reactivation of the steep L_3^{ASZ}–S_3^{ASZ} fabric originally formed during D_3^{ASZ} but under upper crustal conditions and during motion on the late Tertiary Alpine fault. We also suggest that the difference between middle and upper crustal conditions in D_3^{ASZ} compared to D_4^{ASZ} despite similar dextral strike-slip kinematics could reflect some vertical displacement and exhumation during D_3^{ASZ} transpression. Vertical crustal displacements during ductile transpression are predicted in some pure-shear dominated transpressional systems (Fossen and Tikoff, 1998).

8. Conclusions

Structural, metamorphic, kinematic vorticity, and finite strain data show that two kinematically unrelated episodes of amphibolite facies deformation (D_2^{ASZ} and D_3^{ASZ}) produced mylonitic to ultramylonitic fabrics in the Anita Shear Zone. These mylonites are superimposed on Paleozoic or early Mesozoic structures (D_1^{SAG}/D_1^{ARC}) preserved in the wall rocks of the shear zone. D_2^{ASZ} occurred within a lower crustal (~40 km depth) thinning, simple shear-dominated flow regime ($W_k = 0.84$) resulting in top-down-to-the-SE normal displacements. Peak metamorphic conditions during D_2^{ASZ} were calculated at 11.9 ± 1.1 kbar and 581 ± 34°C. The L_2^{ASZ}–S_2^{ASZ} fabric is sharply truncated and overprinted by a steep to subvertical fabric (L_3^{ASZ}–S_3^{ASZ}) that preserves evidence for major subhorizontal (NNE–SSW) dextral displacement at high angles to the L_2^{ASZ} transport direction. Finite strain data also show that both D_2^{ASZ} and D_3^{ASZ} deformation approximated plane strain conditions with D_2^{ASZ}

reflecting slightly more constrictional strains and D_3^{ASZ} reflecting slightly more flattening strains. Peak metamorphic conditions during D_3^{ASZ} were calculated at 8.7 ± 1.2 kbar and 587 ± 42°C. L_3^{ASZ}–S_3^{ASZ} formed within a dextral, pure shear-dominated, mid-crustal transpressional flow regime ($W_k = 0.54$). In addition to dextral displacements, this deformation resulted in a strong component of horizontal shortening perpendicular to the NNE-trending subvertical boundaries of the shear zone.

These data indicate that, during D_2^{ASZ}, the Anita Shear Zone was a lower crustal ductile normal fault that contributed to thinning of the lower crust, decompression and rapid, isothermal exhumation of rocks from ~40 km depth to ~30 km depth prior to the onset of D_3^{ASZ}. Available data also suggest that D_2^{ASZ} occurred during or after mid-Cretaceous extensional deformation in central Fiordland and upper crustal normal faulting in the Nelson–Westland region. Continued decompression, vertical uplift and exhumation of the shear zone from mid- to upper-crustal levels may also have occurred during D_3^{ASZ} transpression. D_3^{ASZ} appears to have resulted from latest Cretaceous or early Tertairy oblique convergence during the last stages of the opening of the Tasman Sea. The differences between D_2^{ASZ} and D_3^{ASZ} reflect changing tectonic regimes during late Mesozoic to Cenozoic tectonism in northern Fiordland. Late greenschist facies, cataclastic shear zones and brittle faults (D_4^{ASZ}) within the Anita Shear Zone record an upper crustal reactivation by dextral strike-slip faults and narrow shear zones that strongly resemble late Tertiary deformation patterns associated with the southernmost segment of the Australian–Pacific transform plate boundary.

Acknowledgements

Funding to support this work was provided by two University of Sydney Institutional Australian Research Council grants to K. A. Klepeis. An Australian post-graduate award supported N. Daczko during preparation of this manuscript. We are grateful to Richard White for his valuable assistance in the field; to Nick Mortimer and Andy Tulloch of the IGNS, Dunedin for helpful discussions, and to the Department of Conservation in Te Anau for permission to visit and sample localities in the Fiordland National Park. Thanks also go to Tim Patrick, Julie Hollis and Helen Degeling for their assistance in the field. B. Tikoff kindly provided us with a computer program to help plot our strain data in 3D. We thank Nick Mortimer, Marcia Bjørnerud, and Richard Norris for helpful suggestions on improving the manuscript.

References

Blattner, P., 1991. The North Fiordland transcurrent convergence. New Zealand Journal of Geology and Geophysics 34, 533–542.

Bobyarchick, A.R., 1986. The eigenvalues of steady flow in Mohr space. Tectonophysics 122, 35–51.

Bradshaw, J.Y., 1989. Origin & metamorphic history of an Early Cretaceous polybaric granulite terrain, Fiordland, southwest New Zealand. Contributions to Mineralogy and Petrology 103, 346–360.

Bradshaw, J.Y., 1990. Geology of crystalline rocks of northern Fiordland: details of the granulite facies Western Fiordland Orthogneiss & associated rock units. New Zealand Journal of Geology and Geophysics 33, 465–484.

Brown, E.H., 1996. High-pressure metamorphism caused by magma loading in Fiordland, New Zealand. Journal of Metamorphic Geology 14, 441–452.

Carter, R.M., Landis, C.A., Norris, R.J., Bishop, D.G., 1974. Suggestions towards a high-level nomenclature for New Zealand rocks. Journal of the Royal Society of New Zealand 4, 29–84.

De Paor, D.G., 1988. R_f/ϕ_f strain analysis using an orientation net. Journal of Structural Geology 10, 323–333.

De Paor, D.G., Simpson, C., 1995. R_f/Fry v.2.0.6 user manual. © 1987–1995 Earth'n'Ware Inc.

Fossen, H., Tikoff, B., 1998. Extended models of transpression and transtension, and application to tectonic settings. In: Holdsworth, R.E., Strachan, R.A., Dewey, J.F. (Eds.), Continental Transpressional and Transtensional Tectonics, Special Publications 135. Geological Society, London, pp. 15–33.

Freeman, B., 1985. The motion of rigid ellipsoidal particles in slow flows. Tectonophysics 113, 163–183.

Gaina, C., Müller, D.R., Royer, J.-Y., Stock, J., Hardebeck, J., Symonds, P., 1998. The tectonic history of the Tasman Sea: A puzzle with thirteen pieces. Journal of Geophysical Research 103, 12413–12433.

Ghosh, S.K., 1993. Structural Geology: Fundamentals and Modern Developments. Pergamon Press, Oxford.

Ghosh, S.K., Ramberg, H., 1976. Reorientation of inclusions by combinations of pure and simple shear. Tectonophysics 34, 1–70.

Gibson, G.M., 1990. Uplift and exhumation of middle and lower crustal rocks in an extensional tectonic setting, Fiordland, New Zealand. In: Fountain, M.H., Salisbury, D.M. (Eds.), Exposed Cross-Sections of the Continental Crust. Kluwer Academic, Dordrecht, pp. 71–101.

Gibson, G.M., Ireland, T.R., 1995. Granulite formation during continental extension in Fiordland. Nature 375, 479–482.

Gibson, G.M., Ireland, T.R., 1996. Extension of Delamarian (Ross) orogen into western New Zealand: Evidence from zircon ages and implications for crustal growth along the Pacific margin of Gondwana. Geology 24, 1087–1090.

Gibson, G.M., McDougall, I., Ireland, T.R., 1988. Age constraints on metamorphism and the development of a metamorphic core complex in Fiordland, southern New Zealand. Geology 16, 405–408.

Hill, E.J., 1995a. A deep crustal shear zone exposed in western Fiordland, New Zealand. Tectonics 14, 1172–1181.

Hill, E.J., 1995b. The Anita Shear Zone: a major, middle Cretaceous tectonic boundary in northwestern Fiordland. New Zealand Journal of Geology and Geophysics 38, 93–103.

Holland, T.J.B., 1993. AX computer program, version AX95. shareware — http://www.esc.cam.ac.uk/software.html.

Holland, T.J.B., Powell, R., 1990. An enlarged and updated internally consistent thermodynamic dataset with uncertainties and correlations; the system K_2O–Na_2O–CaO–MgO–MnO–FeO–Fe_2O_3–Al_2O_3–TiO_2–SiO_2–C–H_2O–O_2. Journal of Metamorphic Geology 8, 89–124.

Ireland, T.R., Gibson, G.M., 1998. SHRIMP monazite and zircon geochronology of high-grade metamorphism in New Zealand. Journal of Metamorphic Geology 16, 149–167.

Jeffrey, G.B., 1923. The motion of ellipsoidal particles immersed in a viscous fluid. Proceedings of the Royal Society of London A102, 161–179.

Klepeis, K.A., Lawver, L.A., 1996. Tectonics of the Antarctic–Scotia plate boundary near Elephant and Clarence islands, West Antarctica. Journal of Geophysical Research 101, 20211–20231.

Klepeis, K.A., Crawford, M.L., Gehrels, G., 1998. Structural history of the crustal-scale Coast shear zone north of Portland Canal, southeast Alaska and Britsh Columbia. Journal of Structural Geology 20, 883–904.

Lamarche, G., Collot, J.-Y., Wood, R.A., Sosson, M., Sutherland, R., Delteil, J., 1997. The Oligocene–Miocene Pacific–Australia plate boundary, south of New Zealand: Evolution from oceanic spreading to strike-slip faulting. Earth and Planetary Science Letters 148, 129–139.

Lawver, L.A., Gahagan, L., 1994. Simplified Cenozoic Antarctic–Australian–New Zealand Tectonics. EOS Transactions of the American Geophysical Union 73, 609.

Lisle, R.J., 1985. Geological Strain Analysis: A Manual for the R_f/ϕ Technique. Pergamon Press, Oxford.

Lister, G.S., Williams, P.F., 1983. The partitioning of deformation in flowing rock masses. Tectonophysics 49, 37–78.

Mattinson, J.L., Kimbrough, D.L., Bradshaw, J.Y., 1986. Western Fiordland orthogneiss: Early Cretaceous arc magmatism and granulite facies metamorphism, New Zealand. Contributions to Mineralogy and Petrology 92, 383–392.

McCulloch, M.T., Bradshaw, J.Y., Taylor, S.R., 1987. Sm–Nd and Rb–Sr isotopic and geochemical systematics in Phanerozoic granulites form Fiordland, Southwest New Zealand. Contributions to Mineralogy and Petrology 97, 183–195.

Mortimer, N., 1993. Jurassic tectonic history of the Otago schists, New Zealand. Tectonics 12, 237–244.

Norris, R.J., Koons, P.O., Cooper, A.F., 1990. The obliquely-convergent plate boundary in the South Island of New Zealand: implications for ancient collision zones. Journal of Structural Geology 12, 715–725.

Oliver, G.J.H., 1980. Geology of the granulite and amphibolite facies gneisses of Doubtful Sound, Fiordland, New Zealand. New Zealand Journal of Geology and Geophysics 1, 27–41.

Oliver, G.J.H., Coggon, J.H., 1979. Crustal structure of Fiordland, New Zealand. Tectonophysics 54, 253–292.

Owens, W.H., 1984. The calculation of a best-fit ellipsoid from elliptical sections on arbitrarily oriented planes. Journal of Structural Geology 6, 571–578.

Passchier, C.W., 1986. Flow in natural shear zones — the consequences of spinning flow regimes. Earth Planetary Science Letters 77, 70–80.

Passchier, C.W., 1987. Stable positions of rigid objects in non-coaxial flow — a study in vorticity analysis. Journal of Structural Geology 9, 679–690.

Passchier, C.W., Urai, J.L., 1988. Vorticity and strain analysis using Mohr diagrams. Journal of Structural Geology 10, 755–763.

Powell, R., Holland, T.J.B., 1988. An internally consistent dataset with uncertainties and correlations: 3. Applications to geobarometry, worked examples and a computer program. Journal of Metamorphic Geology 6, 173–204.

Powell, R., Holland, T.J.B., 1994. Optimal geothermometry and geobarometry. American Mineralogist 75, 367–380.

Simpson, C., De Paor, D.G., 1993. Strain and kinematic analysis in general shear zones. Journal of Structural Geology 15, 1–20.

Simpson, C., Schmid, S.M., 1983. An evolution of criteria to determine the sense of movement of sheared rocks. Geological Society of America Bulletin 94, 1281–1288.

Srivastava, H.B., Hudleston, P., Earley III, D., 1995. Strain and possible volume loss in a high-grade ductile shear zone. Journal of Structural Geology 17, 1217–1231.

Sutherland, R., 1995. The Australia–Pacific boundary and Cenezoic plate motions in the SW Pacific: Some constraints from Geosat data. Tectonics 14, 819–831.

Tikoff, B., Fossen, H., 1995. The limitations of three-dimensional kinematic vorticity analysis. Journal of Structural Geology 17, 1771–1784.

Tulloch, A.J., Kimbrough, D.L., 1989. The Paparoa metamorphic core complex, New Zealand: Cretaceous extension associated with fragmentation of the Pacific margin of Gondwana. Tectonics 8, 1217–1234.

Wallis, S., 1995. Vorticity analysis and recognition of ductile extension in the Sanbagawa belt, SW Japan. Journal of Structural Geology 17, 1077–1093.

Wood, B.L., 1972. Metamorphosed ultramafites and associated formations near Milford Sound, New Zealand. New Zealand Journal of Geology and Geophysics 15, 88–127.